

# The Role of Integration Cycles in Complex Langevin Simulations

Michael W. Hansen,<sup>1,\*</sup> Michael Mandl,<sup>1,†</sup> Erhard Seiler,<sup>2,‡</sup> and Dénes Sexty<sup>1,§</sup>

<sup>1</sup>*Institute of Physics, NAWI Graz, University of Graz, Universitätsplatz 5, 8010 Graz, Austria*

<sup>2</sup>*Max-Planck-Institut für Physik (Werner-Heisenberg-Institut), Boltzmannstraße 8, 85748 Garching bei München, Germany*

Complex Langevin simulations are an attempt to solve the sign (or complex-action) problem encountered in various physical systems of interest. The method is based on a complexification of the underlying degrees of freedom and an evolution in an auxiliary time dimension. The complexification, however, does not come without drawbacks, the most severe of which is the infamous ‘wrong convergence’ problem, stating that complex Langevin simulations sometimes fail to produce correct answers despite their apparent convergence. It has long been realized that wrong convergence may – in principle – be fixed by the introduction of a suitable kernel into the complex Langevin equation, such that the conventional correctness criteria are met. However, as we discuss in this work, complex Langevin results may – especially in the presence of a kernel – still be affected by unwanted so-called integration cycles of the theory spoiling them. Indeed, we confirm numerically that in the absence of boundary terms the complex Langevin results are given by a linear combination of such integration cycles, as put forward by Salcedo & Seiler [1]. In particular, we shed light on the way different choices of kernel affect which integration cycles are being sampled in a simulation and how this knowledge can be used to ensure correct convergence in simple toy models.

## I. INTRODUCTION

Lattice field theory is the most successful method to date for studying nonperturbative aspects of quantum field theory from first principles. One of its major achievements, for instance, is the discovery that the finite-temperature transition in Quantum Chromodynamics (QCD) is, in fact, an analytic crossover [2]. The fact that the temperature axis of the QCD phase diagram is so well understood by now is owed to a large extent to lattice simulations by various collaborations around the globe.

Conventional lattice field theory simulations are based on the idea of importance sampling, by which the Boltzmann factor  $e^{-S_E}$  in the Euclidean path integral (with  $S_E$  denoting the Euclidean action of the theory under study) is interpreted as a probability density from which one draws samples of field configurations. This approach, however, fails if  $S_E$  has a nonvanishing imaginary part since then this probabilistic interpretation breaks down. This is the case, for instance, in QCD with a nonzero baryon chemical potential, which is the reason why straightforward lattice simulations using importance sampling cannot be applied to the study of QCD at finite baryon density [3]. This so-called sign (or complex action) problem is not just restricted to finite-density QCD but is also present in various other systems, such as real-time quantum field theory or gauge theories with a  $\theta$  term.

Needless to say, there are countless attempts for solving or at least mitigating the sign problem, which can be

roughly classified into the following categories: reweighting (e.g., classical reweighting [4] or density-of-states [5] methods), reformulation of theories in terms of new variables (e.g., the worldline approach [6]), methods based on complexification of the underlying field manifold (e.g., the complex Langevin [7, 8] or Lefschetz thimble [9] approaches) or approaches based on the Hamiltonian formalism (e.g., tensor networks [10]). Moreover, for QCD in the presence of a (baryon) chemical potential  $\mu$ , two of the most successful methods that are commonly employed are the analytic continuation from simulations at imaginary  $\mu$ , for which there is no sign problem [11], and Taylor expansions in  $\mu/T$  (with  $T$  denoting the temperature) around  $\mu = 0$  [12].

While all of these ideas come with their own advantages as well as drawbacks, in this work we shall focus on the complex Langevin approach. Based on extending the idea of stochastic quantization [13] (see also [14, 15] for reviews) to complex actions, this method found some success initially [16–19] but was largely discarded afterwards as it caused problems that seemed insurmountable [20–23] at the time. However, the idea re-emerged in an attempt to enable simulations of real-time quantum field theories out of equilibrium [24, 25] and has been developed further since. In particular, the addition of adaptive step-size algorithms [26] and gauge cooling [27] to the complex-Langevin toolbox enabled exploratory studies of finite-density QCD [28–32] as well as the determination of the phase diagram of heavy-dense QCD [33]; see also [34] for a recent review.

Moreover, important progress has been made in assessing the convergence properties of complex Langevin simulations [35–38]. In particular, the study of boundary terms has shed some light on the question why the complex Langevin evolution sometimes produces incorrect results despite a reasonable convergence [39, 40]. However, it has also become clear that boundary terms on their

\* michael.hansen@uni-graz.at

† michael.mandl@uni-graz.at

‡ ehs@mpp.mpg.de

§ denes.sexty@uni-graz.at

own are in general not sufficient as a correctness criterion [41]. Indeed, it was shown in [1] that (at least in one dimension) the absence of boundary terms does not guarantee correct convergence, but only implies that the results obtained in a simulation are linear combinations involving different so-called integration cycles (using the terminology of [42, 43]).

In this work, we shall elaborate more on the role played by integration cycles in the context of complex Langevin simulations and, in particular, how the introduction of a kernel into the Langevin equation can affect this picture. In Sec. II we introduce the (complex) Langevin equation as well as the concept of boundary terms. We then devote Sec. III to a thorough discussion of integration cycles before outlining our simulation setup in Sec. IV. There, we also briefly describe our efforts regarding the reproducibility of our results along the FAIR guiding principles [44]. Lastly, in Sec. V, we present simulation results for simple one- and two-dimensional toy models to elucidate the relation between the kernel and the cycles that are being sampled in simulations. A number of auxiliary results are provided in the appendices.

## II. COMPLEX LANGEVIN EVOLUTION

As was mentioned in the Introduction, the sign problem in lattice quantum field theory arises when the weight  $\rho[x] := e^{-S[x]}/Z$  (here and in the remainder of this work we shall drop the subscript ‘ $E$ ’) in the path integral is not real and non-negative. Here, the partition function  $Z$  is defined as

$$Z := \int_M \mathcal{D}x e^{-S[x]}, \quad (1)$$

where  $x$  collectively denotes all dynamical degrees of freedom of the theory of interest, which may take values in, e.g., the set of real numbers or some real Lie group. We denote the integration manifold as  $M$  and let  $\int_M \mathcal{D}x$  indicate a suitable integration over all possible field configurations of  $x$ . Expectation values of operators  $\mathcal{O}[x]$ , which we shall henceforth simply refer to as observables, are then defined as

$$\langle \mathcal{O} \rangle := \int_M \mathcal{D}x \mathcal{O}[x] \rho[x]. \quad (2)$$

The idea behind the complex Langevin approach is to avoid having to deal with a complex weight  $\rho[x]$  by analytically continuing the action and observables in  $x$  and instead consider field configurations  $z$  of complexified degrees of freedom. For this to work, both  $S$  and  $\mathcal{O}$  are required to be holomorphic. We then denote the complexified manifold, on which the components of  $z$  are defined, as  $M^c$ . As we shall discuss below, the complex Langevin evolution gives rise to a real probability density  $P[z]$ , from which it allows one to draw samples, thus avoiding the sign problem. The crucial point is the question whether or not  $P[z]$  is equivalent to  $\rho[x]$  in the sense

that

$$\int_{M^c} \mathcal{D}z \mathcal{O}[z] P[z] \stackrel{?}{=} \int_M \mathcal{D}x \mathcal{O}[x] \rho[x], \quad (3)$$

or, in other words, whether the expectation values computed in a complex Langevin simulation reproduce the correct values  $\langle \mathcal{O} \rangle$ . As we shall see, this equivalence can – in general – not be guaranteed.

### A. Basic formalism

The complex Langevin approach makes use of the evolution of the complexified degrees of freedom  $z$  in an auxiliary time direction, the so-called Langevin time  $\tau$ . In the following, we consider a single complex degree of freedom,  $z = x + iy$ . The  $\tau$ -evolution of  $z$  is then given by the following (complex) Langevin equation:

$$dz(\tau) = D(z)d\tau + \sqrt{K}dw(\tau), \quad D(z) = -KS'(z). \quad (4)$$

It is a stochastic differential equation in which  $dw$  denotes the increment of a standard Wiener process such that

$$\langle dw(\tau) \rangle = 0, \quad \langle dw^2(\tau) \rangle = 2d\tau \quad (5)$$

and  $K \in \mathbb{C}$  is a so-called kernel whose purpose is to introduce a nontrivial diffusion into the Langevin equation. We have assumed it to be independent of  $z$  (and  $\tau$ ) here for simplicity.

The stochastic evolution of  $z$  in  $\tau$  gives rise to a probability density  $P(x, y; \tau)$  in the complex plane, whose time-evolution is, in turn, given by the Fokker–Planck equation

$$\frac{\partial P(x, y; \tau)}{\partial \tau} = L^T P(x, y; \tau), \quad (6)$$

where we have defined the (real) Fokker–Planck operator  $L^T := \partial_x^2 - \partial_x \text{Re } D - \partial_y \text{Im } D$ . It is a well-known fact that the complexification from  $M$  to  $M^c$  leads to a certain loss of mathematical rigor within the approach. In fact, while the convergence of the Fokker–Planck equation to the desired equilibrium distribution can be shown under rather mild assumptions in the case of a real action, the situation is less clear for complex actions. Additionally, in real Langevin simulations the introduction of a (real) kernel does not alter the equilibrium distribution, whereas for complex actions a complex kernel generally does.

One problem that may arise is the emergence of so-called runaway trajectories. The existence of these (classical) trajectories can cause the  $\tau$ -evolution of  $z$  in the complex plane to wander far away from the real axis, which might bias sample averages and, if not accounted for, even lead to divergent simulations. As an example, consider the theory  $S(z) = z^4$ . Starting from an initial value  $z_0 = iy_0$  (with arbitrary  $y_0 \neq 0$ ), the classical evolution (i.e., the evolution without the noise term  $dw$  in (4)) with a trivial kernel,  $K = 1$ , will diverge. The

noise term will, in general, kick the stochastic evolution off such a runaway trajectory, but, in practice, results might still be biased if a simulation spends too much (Langevin) time far away from the real line, where discretization effects might become significant. As a partial cure, one nowadays commonly uses an adaptively controlled Langevin time step [26] in the discretized evolution equations, which in many cases solves the runaway problem. Either way, runaway trajectories can at the very least be detected, namely by monitoring the distance of  $z(\tau)$  to the real axis in a suitable way. For instance, in the above example one could simply keep track of  $\text{Im } z$  in order to see whether runaway trajectories cause any problems.

The second major problem of complex Langevin simulations cannot be detected in such a straightforward way. Namely, the equilibrium distribution obtained from the Fokker–Planck evolution (6),

$$P(z) := \lim_{\tau \rightarrow \infty} P(x, y; \tau), \quad (7)$$

might not reproduce the correct expectation values  $\langle \mathcal{O} \rangle$ , i.e., it might violate (3). We shall devote the next subsection to a more detailed discussion of this problem.

### B. Boundary terms

First of all, one might ask whether a given  $\rho(z)$  actually admits the existence of any  $P(z)$  satisfying (3) at all. As was shown in [45–47], however, this is indeed the case for rather general  $\rho(z)$ . Whether complex Langevin simulations are capable of producing such a  $P(z)$  is, of course, an entirely different question. A formal proof of correctness of the complex Langevin approach, i.e., of (3), was given in [36]. This proof, however, relies on the sufficiently fast decay of certain quantities, e.g., the probability density  $P(x, y; \tau)$ , in the complex plane, such that one may perform an integration by parts without the appearance of boundary terms. However, it turns out that such boundary terms are, in fact, present quite generally.

A major advance was the realization that the presence of boundary terms in a complex Langevin simulation can be detected by measuring certain auxiliary observables [39, 40]. In particular, the boundary term expectation value for an observable  $\mathcal{O}$  can be defined for a single degree of freedom  $z$  as

$$\mathcal{B}_{\mathcal{O}}(Y) := \langle \Theta(Y - \mathcal{N}(z)) L_c \mathcal{O}(z) \rangle, \quad (8)$$

where we have introduced  $L_c := (\partial_z - S'(z))K\partial_z$ ,  $\mathcal{N}(z)$  denotes a suitable norm of  $z$  and the Heaviside  $\Theta$  function is used to control the spread of the distribution of  $z$  in the complex plane. In practice, one looks for a plateau of  $\mathcal{B}_{\mathcal{O}}(Y)$  in the cutoff  $Y$  and extrapolates to  $Y \rightarrow \infty$ , as  $\mathcal{B}_{\mathcal{O}}$  tends to be very noisy when evaluated directly at  $Y = \infty$ . If such a plateau occurs at a nonvanishing value of  $\mathcal{B}_{\mathcal{O}}$ , one concludes that boundary terms are present and hence the assumptions underlying the proof in [36]

do not hold. This, in turn, implies that the complex Langevin estimate for the expectation value of  $\mathcal{O}$ , which we henceforth denote as  $\langle \mathcal{O} \rangle_{\text{CL}}$ , does not agree with the correct result  $\langle \mathcal{O} \rangle$  and should therefore be discarded. Indeed, the study of boundary terms to assess the correctness of complex Langevin results has become a standard by now [48–51]. We mention that smaller boundary terms are usually associated with a smaller deviation between  $\langle \mathcal{O} \rangle_{\text{CL}}$  and  $\langle \mathcal{O} \rangle$ .

It is important to note that, while the presence of boundary terms can be safely interpreted as wrong convergence (if the stochastic evolution converges at all), i.e., the probability density  $P(z)$  emerging from a simulation not satisfying (3), the converse is not necessarily true. Indeed, the absence of boundary terms is only a necessary requirement for correct convergence, not a sufficient one. A simple counterexample is discussed in [52]. This issue is particularly relevant in the presence of a kernel, and in the remainder of this work we shall discuss it in more detail.

## III. INTEGRATION CYCLES

### A. General considerations

In [22], the wrong convergence of complex Langevin simulations was traced back to the fact that the (complex) Fokker–Planck equation in general features multiple solutions in the space of distributions, all of which may be sampled in a simulation. This observation was later formalized in [1] in the form of a theorem that provides a sound explanation for incorrect convergence despite the absence of boundary terms in one-dimensional theories.

Concretely, [1] considers integration paths in the complex plane that either connect two distinct zeros of  $\rho(z) = e^{-S(z)}$  (with  $S(z)$  denoting the action of a theory analytically continued to complex arguments) or are closed and noncontractible. In the following, we shall refer to such paths as *integration cycles*<sup>1</sup>, thereby borrowing terminology used in [42, 43]. The main statement of [1] is that any linear functional that satisfies the Dyson–Schwinger equations of a one-dimensional theory with an action  $S$  on a suitable space of test functions is given by a linear combination of integrals along such integration cycles; see also [53–55] for previous studies on the role of integration cycles in the context of Dyson–Schwinger equations. The relevance of this theorem for the complex Langevin approach can be appreciated by first realizing that the complex Langevin estimate  $\langle \mathcal{O} \rangle_{\text{CL}}$  for the expectation value of an observable  $\mathcal{O}(z)$  is precisely

<sup>1</sup> More rigorously, an integration cycle is an equivalence class of such paths or, in the language of algebraic topology, a so-called relative homology cycle [42]. In this work, however, we shall refrain from using that terminology.

such a linear functional, defined via the left-hand side of (3). Second, the absence of boundary terms in a complex Langevin simulation is assumed to imply the validity of the aforementioned Dyson–Schwinger equations.

Defining the expectation value of an observable  $\mathcal{O}$  along some integration cycle  $\gamma_i$  as

$$\langle \mathcal{O} \rangle_{\gamma_i} := \frac{\int_{\gamma_i} dz \mathcal{O}(z) e^{-S(z)}}{\int_{\gamma_i} dz e^{-S(z)}}, \quad (9)$$

the theorem thus states that  $\langle \mathcal{O} \rangle_{\text{CL}}$ , obtained in a simulation with vanishing boundary terms, is a linear combination of the  $\langle \mathcal{O} \rangle_{\gamma_i}$ , i.e.,

$$\langle \mathcal{O} \rangle_{\text{CL}} = \sum_{i=1}^{N_\gamma} a_i \langle \mathcal{O} \rangle_{\gamma_i}. \quad (10)$$

Here,  $a_i$  are complex coefficients, which, importantly, are the same for all observables  $\mathcal{O}$ , and  $N_\gamma$  denotes the number of linearly independent integration cycles of the theory. Notice that (10) immediately implies

$$\sum_{i=1}^{N_\gamma} a_i = 1, \quad (11)$$

which can be used as a consistency check.

In practice, one is usually interested in computing the average along some given integration cycle, which could be the real line for instance. Defining  $\gamma_1$  to denote this integration cycle of interest, (10) states that in general a complex Langevin simulation may – even in the absence of boundary terms – not produce the desired result  $\langle \mathcal{O} \rangle_{\gamma_1}$ , but also contributions from the other integration cycles  $\gamma_{i \neq 1}$ . The obvious question that arises is in which situations one may find  $a_i = \delta_{i1}$ , such that  $\langle \mathcal{O} \rangle_{\text{CL}} = \langle \mathcal{O} \rangle_{\gamma_1}$ . In this work, we aim at shedding some light on this question. In particular, we demonstrate that the coefficients  $a_i$  can – in principle – be controlled by the kernel  $K$  in (4). For the simple theories considered here, this can even be done in a rather systematic way. Indeed, since for these models  $\langle \mathcal{O} \rangle_{\gamma_i}$  can be computed directly for a sufficiently large set of observables  $\mathcal{O}$ , we may simply extract the  $a_i$  from (10) via a least-squares fit. For more complicated theories, this is, of course, not possible. In fact, in general one does not even know what the independent integration cycles  $\gamma_i$  are, nor could one hope to compute  $\langle \mathcal{O} \rangle_{\gamma_i}$  directly.

We emphasize that the theorem (10) was proven only for a single degree of freedom. While the concept of integration cycles can be extended to an arbitrary number of dimensions  $d$  in a straightforward way, the validity of (10) beyond  $d = 1$  has not yet been established. In the remainder of this work, we thus investigate the theorem in both one and two dimensions from a numerical point of view. Before doing so, however, we first illustrate the main ideas behind integration cycles, including their linear independence, in a one-dimensional toy model. Moreover, we present an algorithm for counting the number of

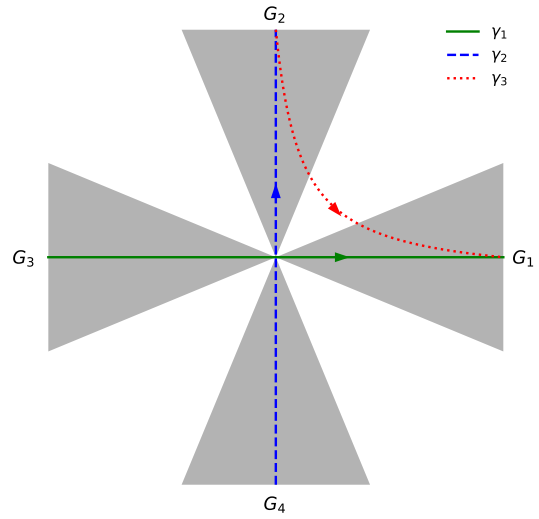


FIG. 1. Topography of  $e^{-S(z)}$  in the complex  $z$  plane. The shaded areas are the regions  $G_i$  defined in (12). Possible realizations of the three independent integration cycles in (14) are shown as full, dashed, and dotted lines, respectively.

independent integration cycles in a certain class of theories with an arbitrary number of degrees of freedom in Appendix A.

## B. One-dimensional example

Let us consider the theory defined by  $S(z) = z^4$ , with  $z \in \mathbb{C}$ , as an example. The density  $\rho(z) = e^{-S(z)}$  vanishes in four disjoint regions as  $|z| \rightarrow \infty$ . Namely, introducing polar coordinates  $z = re^{i\theta}$ ,  $\rho(z)$  approaches zero in the limit  $r \rightarrow \infty$  if and only if  $\theta \in G_i$ , where

$$\begin{aligned} G_1 &= \left(-\frac{\pi}{8}, \frac{\pi}{8}\right), & G_2 &= \left(\frac{3\pi}{8}, \frac{5\pi}{8}\right), \\ G_3 &= \left(\frac{7\pi}{8}, \pi\right] \cup \left(-\pi, -\frac{7\pi}{8}\right), & G_4 &= \left(-\frac{5\pi}{8}, -\frac{3\pi}{8}\right), \end{aligned} \quad (12)$$

see Fig. 1. In particular, each of these regions contains one of the limits  $z \rightarrow \pm\infty$  and  $z \rightarrow \pm i\infty$ , respectively. Since  $\rho(z)$  has no singularities, the set of integration cycles is made up of those paths that connect two different such regions. Moreover, since we consider only holomorphic observables, due to Cauchy's theorem an integration cycle is uniquely specified by the two regions  $G_i$  it connects, i.e., it neither depends on the precise shape of the integration path nor on which exact point within the  $G_i$  (at  $|z| = \infty$ ) it starts and ends on. We thus introduce the notation  $\gamma_{ij}$  for the unique integration cycle that connects regions  $G_i$  and  $G_j$  ( $i \neq j$ ) at infinity.

Hence, in the model  $S(z) = z^4$  there is a total of six (twelve if we count different orientations) integration cycles, only  $N_\gamma = 3$  of which, however, are linearly inde-



pendent. This is due to the following identity:

$$\int_{\gamma_{ij}} dz + \int_{\gamma_{jk}} dz = \int_{\gamma_{ik}} dz . \quad (13)$$

Thus, a possible basis of integration cycles for this theory is given by

$$\gamma_1 = \gamma_{31} , \quad \gamma_2 = \gamma_{42} , \quad \gamma_3 = \gamma_{21} , \quad (14)$$

which are homotopic (homologous) to the real line, the imaginary line and an integration path connecting  $i\infty$  and  $\infty$ , respectively. These integration contours are depicted in Fig. 1 as well.

Now consider the theory  $S(z) = \lambda z^4$  with  $\lambda \in \mathbb{C}$ . In this case, the regions  $G_i$  of vanishing  $\rho(z)$  result from those given in (12) after a rotation by  $\arg \sqrt[4]{1/\lambda}$ . With these, one may again define a basis of integration cycles via (14). Unsurprisingly, this implies that the real line defines a valid integration cycle only as long as  $\text{Re } \lambda > 0$ , which has important consequences for the convergence of complex Langevin simulations. These statements shall be discussed in more detail in Sec. V

The generalization to higher-order polynomial actions

$$S(z) = \sum_{n=1}^{N_0} \lambda_n z^n \quad (15)$$

with  $\lambda_{N_0} \neq 0$  is now straightforward. Namely, there are  $N_0$  regions  $G_i$  and thus, due to (13),  $N_0 - 1$  linearly independent integration cycles, which may be found via a similar procedure as outlined above. The generalization to more than one degree of freedom is more involved and discussed in Appendix A.

#### IV. SIMULATION SETUP

In this section, we discuss details of the numerical simulations performed in order to obtain the results presented in Sec. V. In accordance with the FAIR guiding principles [44], we provide access to our simulation data online [56] and furthermore publish our analysis scripts [57]. Our simulation code is also available upon request.

##### A. Discrete Langevin evolution

For our one- and two-dimensional simulations, we employ a discretized version of the Langevin equation (4). We use the following improved update [58] of a configuration<sup>2</sup>  $z_i$ :

$$z_i \rightarrow z_i - \varepsilon \frac{D_i(z) + D_i(z')}{2} + \sqrt{\varepsilon K_i} \eta_i , \quad (16)$$

<sup>2</sup> Here and in the following there is no implicit summation over repeated indices.

where  $i$  labels the degrees of freedom ( $i = 1, \dots, d$ ), the drift  $D_i(z)$  is defined as

$$D_i(z) := K_i \frac{\partial S(z)}{\partial z_i} \quad (17)$$

and we have introduced the auxiliary intermediate configuration

$$z'_i := z_i - \varepsilon D_i(z) + \sqrt{\varepsilon K_i} \eta_i . \quad (18)$$

In the above equations,  $\varepsilon$  denotes the discretized Langevin-time step size and the  $\eta_i$  are independent random variables drawn from a Gaussian distribution (with mean 0 and variance 2) for every update step. To generate the Gaussian random numbers, we employ a Combined Multiple Recursive Generator (CMRG) as described in [59], combined with a standard Box–Muller transformation [60]. Note that for  $d > 1$ , the kernel, chosen to be independent of  $z_i$  here, can be a full matrix  $K_{ij}$  in general. However, we have chosen it to be diagonal,  $K_{ij} = K_i \delta_{ij}$ , in this work for simplicity. The more general case of  $z_i$ -dependent and/or full matrix kernels will be discussed elsewhere.

##### B. Adaptive-step-size algorithm

In order to mitigate the influence of runaway trajectories on our simulations, we determine the step size  $\varepsilon$  adaptively in the following way [26]:

1. Consider the step size  $\varepsilon$  from the previous update.
2. Propose a  $z'_i$  via (18), compute

$$D_{\max} := \max_i \left| \frac{D_i(z) + D_i(z')}{2} \right| \quad (19)$$

and check whether

$$\frac{\mathcal{D}}{2} \leq \varepsilon D_{\max} \leq 2\mathcal{D} , \quad (20)$$

where  $\mathcal{D}$  is some suitably chosen reference value.

3. If  $\varepsilon D_{\max}$  lies outside that interval, multiply  $\varepsilon$  with appropriate powers of 2 until (20) holds. If the step size grows larger than a given upper limit  $\varepsilon_{\max}$  in the process, set  $\varepsilon = \varepsilon_{\max}$ .
4. Go back to step 2 with the new value of  $\varepsilon$  and repeat these steps until (20) is satisfied at first try.

Once we have determined the step size in this way, we insert it into (16) to proceed to the next configuration and move forward in Langevin time by  $\varepsilon$ . We perform this procedure for every update step until the simulation reaches a certain maximum Langevin time  $\tau_{\max}$ , at which it terminates.

## C. Parallelization

In order to reduce statistical uncertainties as much as possible, we utilize the massive parallelization capabilities of modern GPUs via the CUDA application programming interface [61]. In fact, due to the sheer simplicity of the models considered here, we may actually let one entire simulation, in the way outlined above, run on each individual CUDA thread we launch. Naturally, each of these simulations starts from a different random initial configuration and has an independent random-number seed. For a single simulation run, we launch  $N_{\text{sim}} = \mathcal{O}(10^4)$  CUDA threads and we typically perform  $N_{\text{runs}} = \mathcal{O}(10^2)$  such runs for each parameter value we are interested in. Notice that we distinguish between *simulations*, each of which is performed by a single CUDA thread, and *runs*, which consist of  $N_{\text{sim}}$  such simulations each.

Within each run, every simulation terminates at the same  $\tau_{\text{max}}$  and we also ensure that  $\tau_{\text{max}}$  is the same across runs. Moreover, measurements, which are discussed in detail in the next subsection, are performed whenever each simulation in a run has progressed by a Langevin time of  $\tau_{\text{meas}}$ , where  $\tau_{\text{meas}}$  is chosen to agree between different runs as well. We also monitor whether individual simulations diverge, but, due to the employed adaptive step size algorithm, this barely ever happens and its effect can be neglected entirely. However, what may occur on rare occasions is that one or more simulations are slowed down significantly by the adaptive step size algorithm, which, in turn, affects the entire run due to the synchronization of threads before and after measurements.

## D. Measurement

We do not store the full set of configurations produced by each simulation of a given run, as this would exhaust the available storage rather quickly. Instead, we measure observables as follows: Whenever a simulation has run for a (Langevin) time  $\tau_{\text{meas}}$  since the last measurement, it computes all observables  $\mathcal{O}_i$  of interest, which are – after synchronization – averaged over all simulations within the run, i.e., over all CUDA threads involved. Only these (thread-)averages are then written to file in every measurement step. The main disadvantage of this approach is that one loses information about the configurations produced by individual simulations, as well as their correlations. In order to nonetheless gain some insight into the latter, as well as into the thermalization properties of the simulations, we do monitor the timelines of a handful of individual simulations every once in a while. Note that our strategy does not allow us to perform measurements of new observables without re-generating the ensembles from scratch.

### 1. Regular observables

An estimator for the expectation value of an observable,  $\langle \mathcal{O}_i \rangle_{\text{CL}}$ , is computed in the following way: For each run, the (thread-averaged) timeline of  $\mathcal{O}_i$  is read and all measurements up to a Langevin time of  $\tau_{\text{therm}}$  are discarded to account for thermalization. The thermalized timelines are then averaged over Langevin time, leaving us with a total of  $N_{\text{runs}}$  (uncorrelated) data points for each observable. Finally, the estimator  $\langle \mathcal{O}_i \rangle_{\text{CL}}$  is computed as the average of these data points over all runs, while its statistical uncertainty is their standard deviation divided by  $\sqrt{N_{\text{runs}}}$ .

### 2. Boundary terms and histograms

The computation of boundary terms is somewhat trickier, as it has to be done online due to the  $\Theta$  function in (8), information of which is lost after the thread-averaging. We first fix (for all simulations in all runs) a range  $[Y_{\text{min}}, Y_{\text{max}})$  for the cutoff  $Y$ , which we discretize into  $N_Y$  bins logarithmically. After the initial wait time  $\tau_{\text{therm}}$  to ensure thermalization, boundary terms for each observable  $\mathcal{O}_i$  are computed during every measurement step as follows: In each simulation, we compute the norm  $\mathcal{N}(z)$  in (8), defined here as  $\mathcal{N}(z) := \max_i |z_i|$ , to determine the corresponding  $Y$  bin and add the quantity  $L_c \mathcal{O}_i(z)$  to that bin. After the run has finished, the bins are normalized by the number of thermalized measurements,  $N_{\text{meas}} = (\tau_{\text{max}} - \tau_{\text{therm}})/\tau_{\text{meas}}$ , (which is an integer with our choice of parameters) as well as the number of simulations  $N_{\text{sim}}$  in that run. The  $\Theta$  function in (8) is then implemented by adding each  $Y$  bin to all bins that correspond to larger values of  $Y$ . This leaves us with one value of  $B_{\mathcal{O}_i}$  per bin for each run, from which we obtain estimators for the expectation value and uncertainty in the same way as for the regular observables. We also note that histograms of the configurations may be computed in a similar fashion.

### 3. Integration cycle coefficients

In order to determine the coefficients  $a_i$  in (10), we employ the following strategy: First of all, consider the output of a single simulation run, which consists of  $N_{\text{meas}}$  thermalized measurements for each (thread-averaged) observable. The  $\tau$ -average of these quantities thus already provides us with a reasonable estimate  $\overline{\mathcal{O}_i}$  for  $\langle \mathcal{O}_i \rangle_{\text{CL}}$  that we may use in the left-hand-side of (10) to extract the  $a_i$  via a least-squares fit. Defining the number of measured observables as  $N_{\mathcal{O}}$ , we therefore require  $N_{\mathcal{O}} \geq N_{\gamma}$ . Importantly, there are nonnegligible correlations between the observables that we take into account by computing their covariance matrix. In order to do so in a well-defined way, we first split all observables into their real and imaginary parts and consider

those as independent (real) observables. Then, (10) can (with the replacement  $\langle \mathcal{O}_i \rangle_{\text{CL}} \rightarrow \mathcal{O}_i$ ) be written as the matrix equation

$$\mathbf{y} = X\boldsymbol{\beta}, \quad (21)$$

where  $\mathbf{y}$  and  $\boldsymbol{\beta}$  are real vectors with  $2N_{\mathcal{O}}$  and  $2N_{\gamma}$  components, respectively, which are defined as

$$\begin{aligned} y_{2i-1} &= \text{Re } \overline{\mathcal{O}_i}, & y_{2i} &= \text{Im } \overline{\mathcal{O}_i}, & 1 \leq i \leq N_{\mathcal{O}}, \\ \beta_{2j-1} &= \text{Re } a_j, & \beta_{2j} &= \text{Im } a_j, & 1 \leq j \leq N_{\gamma}, \end{aligned} \quad (22)$$

and  $X$  is the  $(2N_{\mathcal{O}} \times 2N_{\gamma})$ -matrix resulting from  $\langle \mathcal{O}_i \rangle_{\gamma_j}$  via

$$\begin{aligned} X_{2i-1,2j-1} &= \text{Re} \langle \mathcal{O}_i \rangle_{\gamma_j}, & X_{2i-1,2j} &= -\text{Im} \langle \mathcal{O}_i \rangle_{\gamma_j}, \\ X_{2i,2j-1} &= \text{Im} \langle \mathcal{O}_i \rangle_{\gamma_j}, & X_{2i,2j} &= \text{Re} \langle \mathcal{O}_i \rangle_{\gamma_j}. \end{aligned} \quad (23)$$

Then, denoting the covariance matrix of  $\mathbf{y}$  (computed as an average over  $\tau$  and normalized by  $1/\sqrt{N_{\text{meas}}}$ ) by  $\Sigma$ , the least-squares estimator  $\hat{\boldsymbol{\beta}}$  is obtained by minimizing

$$\chi^2 := (\mathbf{y} - X\boldsymbol{\beta})^T \Sigma^{-1} (\mathbf{y} - X\boldsymbol{\beta}) \quad (24)$$

and reads

$$\hat{\boldsymbol{\beta}} = (X^T \Sigma^{-1} X)^{-1} X^T \Sigma^{-1} \mathbf{y}. \quad (25)$$

Thus, after deciding on a suitable set of observables, we may compute  $\hat{\boldsymbol{\beta}}$  for every run and obtain a final estimate for the coefficients  $a_i$  and their uncertainties by averaging over runs and computing the standard deviation (divided by  $\sqrt{N_{\text{runs}}}$ ), as before.

### E. Simulation parameters

For the runs discussed in this work, we fix the maximum Langevin time per simulation to  $\tau_{\text{max}} = 1000$  and we store (thread-averaged) measurements after every  $\tau_{\text{meas}} = 0.1$ . The step size is initialized with a value of  $\varepsilon = 10^{-5}$  and not allowed to grow beyond that value, i.e.,  $\varepsilon \leq \varepsilon_{\text{max}} = 10^{-5}$ . The reference value in (20) is chosen to be  $\mathcal{D} = 10^{-2}$ . For each run, we simultaneously launch  $N_{\text{sim}} = 2^{13}$  CUDA threads on  $2^8$  thread blocks and we perform between  $N_{\text{runs}} = 100$  and  $N_{\text{runs}} = 200$  runs for each parameter value of interest. We compute averages after discarding measurements up to a thermalization time of  $\tau_{\text{therm}} = 50$ , after which we also start measuring boundary terms. The range of the cutoff  $Y$  is set to  $[Y_{\text{min}}, Y_{\text{max}}] = [10^{-5}, 40]$  and partitioned into  $N_Y = 200$  bins logarithmically. For a few runs, we moreover compute histograms, for which the same number of configurations is discarded. This is important because unthermalized configurations might wrongly suggest that histograms have power-law tails when they actually decay exponentially.

## V. RESULTS

Let us now turn to the discussion of our simulation results. The first main goal of this investigation is to check the validity of (10) numerically, both in one dimension, where it was proven in [1], and in two dimensions, where it is only a conjecture at this point. Second, we also aim at establishing a relation between the kernel  $K$  in (4) and the coefficients  $a_i$  in (10).

### A. One dimension

To begin with, let us consider the model

$$S(z) = \frac{\lambda}{4} z^4, \quad (26)$$

with a complex coefficient  $\lambda$  that is parametrized by an integer  $l$  as

$$\lambda = e^{i\pi l/6}, \quad l \in \{-5, \dots, 6\}. \quad (27)$$

The effect of a kernel on complex Langevin simulations of this model was first studied in [62] and previous results regarding the relation between a kernel and the theorem (10) in the model can be found in [52].

Our simulation setup was described in detail in Sec. IV. In particular, we use (18) and (16) for the discrete Langevin update step, where, as in [52, 62], we parametrize the kernel as

$$K = e^{i\pi m/24}, \quad m \in \{0, \dots, 47\}. \quad (28)$$

We are interested in computing monomial observables of the form  $\langle z^n \rangle$ ,  $n > 0$ , which in the model (26) can be computed exactly. Indeed, one finds

$$\frac{\int_{-\infty}^{\infty} dz z^{2k} e^{-S(z)}}{\int_{-\infty}^{\infty} dz e^{-S(z)}} = \left(\frac{4}{\lambda}\right)^{\frac{k}{2}} \frac{\Gamma((2k+1)/4)}{\Gamma(1/4)}, \quad (29a)$$

$$\frac{\int_{-\infty}^{\infty} dz z^{2k+1} e^{-S(z)}}{\int_{-\infty}^{\infty} dz e^{-S(z)}} = 0, \quad (29b)$$

for even and odd powers of  $z$ , respectively, where  $k$  is a nonnegative integer and  $\Gamma$  denotes the usual gamma function. Notice that in (29) we integrate over the real axis, such that we require  $\text{Re } \lambda > 0$  (or  $|l| < 3$ ) for the integrals to exist, but one may analytically continue the right-hand side to arbitrary values of  $\lambda \neq 0$ . However, an analytic expression can have ambiguities due to cuts and is generally unavailable. Therefore, as described below, we define the analytic continuation of such integrals by making use of integration cycles, avoiding any such ambiguities.

To this end, we first need to specify precisely what is meant by the generalization of the basis integration cycles (14) for  $\lambda \notin \mathbb{R}$  alluded to in Sec. III B. Concretely, we perform the variable transformation

$$z \rightarrow \sqrt[4]{\lambda} z =: \xi. \quad (30)$$

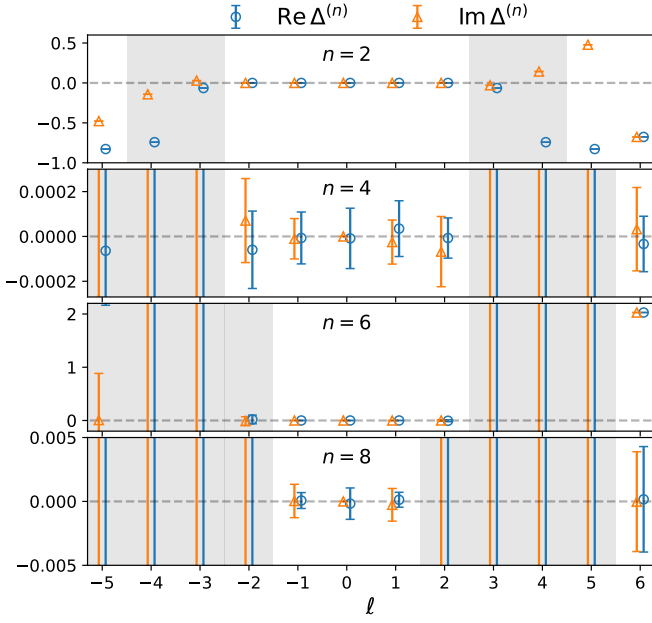


FIG. 2. Real and imaginary parts of the difference  $\Delta^{(n)}$  in (32) for even  $n$  as a function of the integer  $l$  in (27). For values of  $l$  within the shaded regions, the corresponding observable has a nonzero boundary term. Notice the different scales on the vertical axes; the axis limits have been chosen such that all results without boundary terms fit within. The dashed horizontal lines indicate  $\Delta^{(n)} = 0$  and the data points have been displaced horizontally for better visibility.

In the new variable  $\xi$ , the action (26) is real on the real axis for any choice of  $\lambda$ , such that the discussion in Sec. III B applies directly. In particular, we define the linearly independent integration cycles as in (14), except that the integration variable is now  $\xi$  instead of  $z$ . This implies, for instance, that the integration cycle  $\gamma_1$ , which is homotopic to the real  $\xi$  axis (such that we shall sometimes refer to it as the ‘real’ integration cycle), is, in fact, not (homotopic to) a real contour in the original variable  $z$  if  $\lambda \notin \mathbb{R}$ . With this definition and the notation introduced in (9), the right-hand side of (29) is then simply given by  $\langle z^n \rangle_{\gamma_1}$  without requiring any analytic continuation. This leads to a natural definition for the exact result of  $\langle z^n \rangle$  as

$$\langle z^n \rangle_{\text{exact}} := \langle z^n \rangle_{\gamma_1}. \quad (31)$$

In the following, we shall examine under which conditions the result  $\langle z^n \rangle_{\text{CL}}$  obtained in a complex Langevin simulation coincides with  $\langle z^n \rangle_{\text{exact}}$ .

### 1. Trivial kernel

A comparison between  $\langle z^2 \rangle_{\text{CL}}$  and  $\langle z^2 \rangle_{\text{exact}}$ , including a discussion of the corresponding boundary term  $\mathcal{B}_{z^2}$ , for  $K = 1$  (i.e.,  $m = 0$ ) and different values of  $\lambda$  was presented in [52]. Here, we shall discuss this issue in more

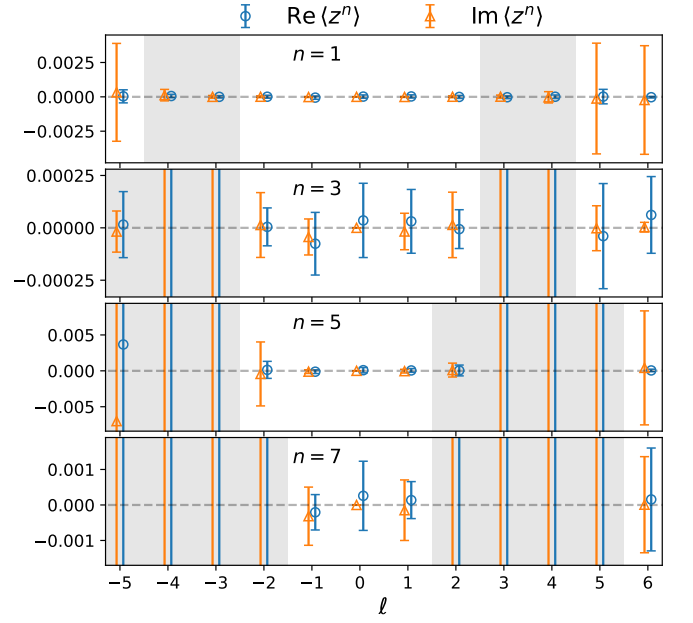


FIG. 3. Real and imaginary parts of the observables  $\langle z^n \rangle_{\text{CL}}$  for odd  $n$  as a function of the integer  $l$  in (27). Otherwise analogous to Fig. 2 (note that  $\Delta^{(n)} = \langle z^n \rangle_{\text{CL}}$  for odd  $n$ ).

detail and consider higher powers in the observables as well. Concretely, we have measured  $\langle z^n \rangle_{\text{CL}}$  and  $\mathcal{B}_{z^n}(Y)$  for  $n \in \{1, \dots, 8\}$ . Defining the difference

$$\Delta^{(n)} := \langle z^n \rangle_{\text{CL}} - \langle z^n \rangle_{\text{exact}}, \quad (32)$$

we compare simulation and exact results for various  $\lambda$  and even values of  $n$  in Fig. 2. For each  $\lambda$  and  $n$ , we moreover look for plateaus in  $Y$  of the corresponding boundary term. If such a plateau is assumed at a value of  $\mathcal{B}_{z^n}$  that differs from zero by more than three times the statistical uncertainty or if there is no clear signal for such a plateau at all, we conclude that there is a nonvanishing boundary term and the result  $\langle z^n \rangle_{\text{CL}}$  must thus be incorrect.<sup>3</sup> For each observable, the values of  $l$  for which we observe signals for boundary terms are indicated by the shaded regions in Fig. 2. Corresponding results for odd  $n$ , for which  $\langle z^n \rangle_{\text{exact}} = 0$ , are shown in Fig. 3. We observe that generically the simulation results show good agreement with  $\langle z^n \rangle_{\text{exact}}$  for values of  $l$  close to zero (or  $\lambda$  close to the positive real axis), where there are no boundary terms.

Obviously, the question whether  $\mathcal{B}_{z^n}(Y)$  shows a plateau at a nonvanishing value may have a different answer for different  $n$ . The statement that boundary terms

<sup>3</sup> Notice that this is not an exact procedure, with the result that the boundaries between regions with  $\mathcal{B}_{z^n} = 0$  and  $\mathcal{B}_{z^n} \neq 0$  are not sharp but might be subject to small variations. However, since smaller boundary terms are typically correlated with smaller deviations from  $\langle z^n \rangle_{\text{exact}}$ , it makes little difference in practice whether boundary terms vanish exactly or are just very small.



are absent, however, requires that such plateaus be consistent with zero for *all* observables. In particular, as becomes clear from Figs. 2 and 3, boundary terms might appear to be consistent with zero for some lower powers of  $z$  but deviate from zero for higher powers. While one might argue that in such a case even the boundary terms for low orders should, in fact, be finite (but small and potentially hard to distinguish from zero), one concludes that it is advisable in general to consider a large set of observables covering a broad range of powers. This is particularly important since the theorem (10) relies on the absence of boundary terms for all observables.

In the earlier study [52], only the boundary terms for  $z^2$  were taken into account. Looking at Figs. 2 and 3, however, this restriction can actually turn out to be misleading in some cases. For instance, the results of [52] suggest that boundary terms are absent for  $l = 5$ , while in reality they become significant only for  $z^n$  with  $n \geq 4$ . In such a case, one should thus not expect (10) to hold. In passing, we mention that, as seen in Figs. 2 and 3, the statistical uncertainties tend to be much larger in the presence of boundary terms, especially for large  $n$ , reflecting the slow decay of the corresponding probability distributions in the complex plane.

We stress that one should not be tempted at this point to interpret the presence of boundary terms as an indication for convergence to ‘incorrect’ results, as one would in simulations of realistic theories. After all, we have not defined what the ‘correct’ results should be – all we do is compare with (29). In that respect, a nonzero boundary term  $\mathcal{B}_{z^n}$  simply means that the associated probability distribution has slowly decaying tails. It is interesting to observe that the resulting large error bars actually in many cases allow for the interpretation that  $\langle z^n \rangle_{\text{CL}}$  could, in fact, be consistent with  $\langle z^n \rangle_{\text{exact}}$ . However, these results are still unusable as they are entirely dominated by noise despite the large amount of statistics in our setup. In other cases, especially for low powers  $n$ , error bars are small but the results nonetheless disagree with  $\langle z^n \rangle_{\text{exact}}$ . These are the two ways in which boundary terms can distinguish between good and bad results.

The crucial point that we would like to emphasize, however, is that – on its own – the absence of boundary terms does not automatically imply that  $\langle z^n \rangle_{\text{CL}} = \langle z^n \rangle_{\text{exact}}$ . The data for  $l = 6$ , for instance, serve as a counterexample, as there is a clear disagreement between the complex Langevin results and (29a) for even powers  $n$ , despite the boundary terms being consistent with zero for all  $n$  considered. This observation shall now be explained as contributions from unwanted integration cycles  $\gamma_{i \neq 1}$ .

In order to compute the coefficients  $a_i$  in (10), we follow the procedure outlined in Sec. IVD, where in the least-squares fit we use the  $N_\gamma = 3$  independent integration cycles (14) and the following set of observables:

$$\{\langle z \rangle, \langle z^2 \rangle, \langle z^4 \rangle, \langle z^5 \rangle, \langle z^6 \rangle, \langle z^8 \rangle\}. \quad (33)$$

In fact, out of the eight observables we have measured,

(33) is the largest set we can use in the fit, since  $\langle z^{4k+3} \rangle_{\gamma_i} = 0$  for all  $i$  and nonnegative integers  $k$ , such that the exact results for  $n = 3$  and  $n = 7$  are trivial and do not provide any usable information. We remark that for the fit we have, in fact, computed  $\langle z^n \rangle_{\gamma_i}$  via numerical integration to be consistent with the two-dimensional case discussed below.

For diagnostic reasons, we have compared fits obtained with different sets of observables, also including exponential observables of the form  $\langle e^{\alpha z^k} \rangle$  (with  $\alpha \in \mathbb{C}$  and  $k$  a positive integer). We found that (in the cases where the fit provides any reasonable result at all), the results are more or less independent of the chosen set as long as the latter is sufficiently large. In particular, our investigations suggest that any set of five or more different observables  $\mathcal{O}$  with at least one nontrivial  $\langle \mathcal{O} \rangle_{\gamma_i}$  will provide consistent results. This is also the reason why we do not consider exponential observables in the remainder of this work. In order to assess the goodness of our fit results, we have analyzed the distribution of whitened residuals in a procedure that is outlined in Appendix B. Whenever we say that a fit is good, we mean that it satisfies the criteria defined there.

In general, we observe that the least-squares fit works well whenever there are no boundary terms but becomes unreliable when boundary terms are nonzero. Indeed, the presence of boundary terms is correlated with the covariance matrix  $\Sigma$  in (25) becoming ill-conditioned, which results in its inversion and, by extension, the fit results becoming unstable. This is exactly the expected behavior, as (10) is valid only in the absence of boundary terms. Note that for  $l = 0$  all simulation trajectories are confined to the real axis after thermalization. In this case, the only integration cycle that is being sampled is  $\gamma_1$ , trivially, without the need of a fit, which is also consistent with (10). In fact, our approach does not allow us to compute the coefficients  $a_i$  in this case, as the imaginary parts of all observables vanish, rendering  $\Sigma$  singular.

The only values of  $l \neq 0$  for which boundary terms vanish with a trivial kernel are  $l = \pm 1, 6$  and we present fit results for the coefficients  $a_i$  for those values in Table I. We observe that  $a_i \approx \delta_{i1}$  as long as  $\lambda$  is sufficiently close to the positive real axis. In other words, for  $|\lambda| < 2$  only the real integration cycle contributes significantly to our simulations with  $K = 1$ , such that the latter reproduce  $\langle z^n \rangle_{\text{exact}}$ , in accordance with Figs. 2 and 3. For  $l = 6$ , on the other hand,  $\gamma_1$  and  $\gamma_2$  both contribute equally, explaining the deviations in Figs. 2 and 3 despite the absence of boundary terms. Importantly, the consistency condition (11) is fulfilled for all values of  $l$  in Table I. We note that the fact that  $\langle z^{4k} \rangle_{\text{CL}} \approx \langle z^{4k} \rangle_{\text{exact}}$  for positive integers  $k$  at  $l = 6$  is because  $\langle z^{4k} \rangle_{\gamma_1} = \langle z^{4k} \rangle_{\gamma_2}$  due to symmetry. Also notice that  $a_3$  is vanishingly small for all  $l$  in Table I, indicating that the third integration cycle  $\gamma_3$  is not sampled at all in our runs, which also explains the agreement between simulation and exact results for odd  $n$ , as  $\langle z^{2k+1} \rangle_{\gamma_1} = \langle z^{2k+1} \rangle_{\gamma_2} = 0$  for nonnegative integers  $k$ . This fact shall be discussed in more detail below.

TABLE I. Coefficients  $a_i$  in the model (26) for  $K = 1$  and different values of  $l$  in (27) for which boundary terms vanish, obtained from (10) via the least squares fit procedure outlined in Sec. IV D 3, using the observables (33). The results are rounded to the first significant digit of the respective statistical uncertainties.

$l$	$a_1$	$a_2$	$a_3$
-1	$1.00003(2) + 0.000006(4)i$	$0.000006(3) - 0.00004(2)i$	$-0.00005(2) + 0.00003(1)i$
1	$1.00000(2) + 0.000003(5)i$	$0.000005(3) + 0.00002(2)i$	$0.00002(1) - 0.00002(2)i$
6	$0.4999(4) - 0.4999(4)i$	$0.5001(4) + 0.5001(4)i$	$-0.00003(1) - 0.0002(8)i$

We conclude that all of our results presented so far are in excellent agreement with the theorem (10). In particular, we observe that as long as boundary terms vanish for all measured observables we obtain stable fits for the coefficients  $a_i$  that also obey (11). Moreover, we have experimented with different basis sets of integration cycles and found consistent results. As an additional test, we have also performed fit analyses based on sets of  $N_\gamma < 3$  integration cycles and find that the fit works as long as the integration cycles that are sampled in a simulation are linear combinations of the cycles used for the fit, which is the expected behavior. When choosing  $N_\gamma > 3$ , on the other hand, fits are no longer reliable since the  $\langle z^n \rangle_{\gamma_i}$  for different  $i$  are not linearly independent in this case.

Overall, our results suggest that the question which linear combination of basis integration cycles is sampled in a complex Langevin simulation of (26) with  $K = 1$  and vanishing boundary terms has a unique answer, which can be found within the statistical uncertainties via an appropriate least-squares fit. In particular, we find the fit to be good (according to the criteria of Appendix B) if and only if it produces this unique answer. Our results thus provide a sound test of the theorem (10), which is found to hold in exactly the way one would expect.

## 2. Nontrivial kernel

We have seen that for most values of  $\lambda$ , measurements in complex Langevin simulations with  $K = 1$  are either affected by boundary terms (i.e., slowly decaying probability distributions) or by the sampling of unwanted integration cycles. However, as is known since [62], the introduction of a nontrivial kernel  $K \approx \lambda^{-1/2}$  in (4) can ensure  $\langle z^n \rangle_{\text{CL}} = \langle z^n \rangle_{\text{exact}}$  for arbitrary  $\lambda \neq 0$ . This is because – in general – a kernel has the effect of rotating the simulation trajectories in a certain way. In fact, as we shall see below, for the choice  $K = \lambda^{-1/2}$  the ensuing probability distribution is confined to a one-dimensional subset of the complex plane, namely the line passing through the origin at an angle given by the argument of  $\lambda^{-1/4}$ . This implies that a simulation with this choice of kernel is equivalent to a real Langevin simulation in the variable  $\xi$  introduced in (30), which can be shown to converge. More generally, the argument of the kernel (or more precisely, the argument of the noise term  $\sqrt{K}\eta$ ) can be expected to govern the orientation of the distribution of  $z$  in the complex plane. This also

means that the kernel, apart from being able to get rid of boundary terms, must also affect the coefficients  $a_i$  in (10) in some way. To the best of our knowledge, the precise way in this happens was first studied in [52]. Here, we shall extend these results.

To this end, we focus on  $l = 5$ , i.e.,  $\lambda = e^{5i\pi/6}$  in (26), but mention that here and in the remainder of this work we may have as well chosen any other value of  $\lambda \neq 0$  with only minor modifications in the analysis. The effect of different kernels, i.e., different values of  $m$  in (28), on the distribution of  $z$  can be appreciated from the histograms shown in Fig. 4. Indeed, we observe that the distributions are aligned roughly parallel to  $\sqrt{K}$ . Note, however, the different shapes of the distributions for different values of  $m$ . Two observations are particularly striking:

First of all, the distribution is confined to a line not only for  $m = 10$ , but for  $m = 34$  as well. Notice that in those cases all simulation trajectories converge to the same line (determined by  $\sqrt{K}$ ) despite the use of random initial conditions. Under closer inspection, it turns out that the two lines sampled for  $m = 10$  and  $m = 34$  are precisely the two stable Lefschetz thimbles<sup>4</sup> of the model (26) for this value of  $\lambda$ . Due to the way we have defined the real integration cycle  $\gamma_1$ , it is thus only natural to conclude that  $m = 10$  is the best choice for reproducing  $\langle z^n \rangle_{\text{exact}}$  in a simulation. In fact, it is a general expectation that if the complex Langevin distribution aligns with the relevant Lefschetz thimbles of the theory, the produced results will likely be correct. For previous studies on the relevance of Lefschetz thimbles within complex Langevin simulations, see, e.g., [49, 63–65].

Second, for certain ranges of  $m$ , for instance around  $m = 0$  or  $m = 24$ , the distributions consist of two disconnected parts separated by a barrier, with a zero transition probability between them in extreme cases. This can happen because the drift vanishes or points away from the barrier in its vicinity, while the noise is perpendicular to it. It results in the loss of ergodicity, implying that a single simulation would be stuck in one of the two regions, depending on the initial conditions, forever,

<sup>4</sup> By a Lefschetz thimble we refer to a one-dimensional subset of the complex plane going through a critical point of the action  $S$  and along which  $\text{Im } S = \text{const.}$ . For the quartic model (26), there are four such thimbles: two stable ones, on which  $\text{Re } S$  increases as  $z$  approaches complex infinity and two unstable ones, on which it decreases.

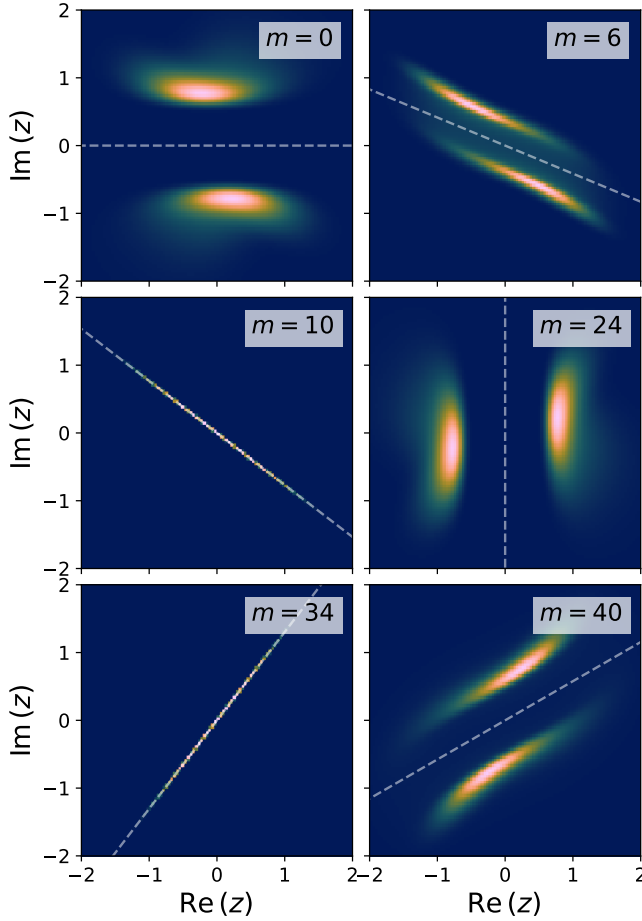


FIG. 4. Histograms of  $z$  in the complex plane, obtained in complex Langevin simulations of the model (26) with  $\lambda = e^{5i\pi/6}$  and different kernels  $K = e^{-mi\pi/24}$ . The brighter regions indicate a higher probability and the dashed lines lie in the direction of the argument of the noise coefficient  $\sqrt{K}$ .

spoiling expectation values. The reason why we nevertheless observe symmetric distributions is that we take the histograms over all our parallel simulations, each of which has randomized initial conditions, in many successive runs.

The latter observation has important consequences for the interpretation of the computed coefficients  $a_i$ , i.e., for the question which integration cycles are sampled in our simulation runs. As a matter of fact, we have verified that one may obtain different results for the  $a_i$  if one uses the same fixed (rather than different randomized) initial conditions for all simulations, such that only one of the two high-probability regions contributes. In particular, in that case one may find  $a_3 \neq 0$ , indicating that individual simulations, which are affected by the ergodicity problem, may actually sample  $\gamma_3$ , even though its contributions cancel in the average over many simulations when randomized initial conditions are used. Indeed, we find  $a_3$  to be vanishingly small in all our simulations with random initial conditions, see, e.g., Table I. The reason

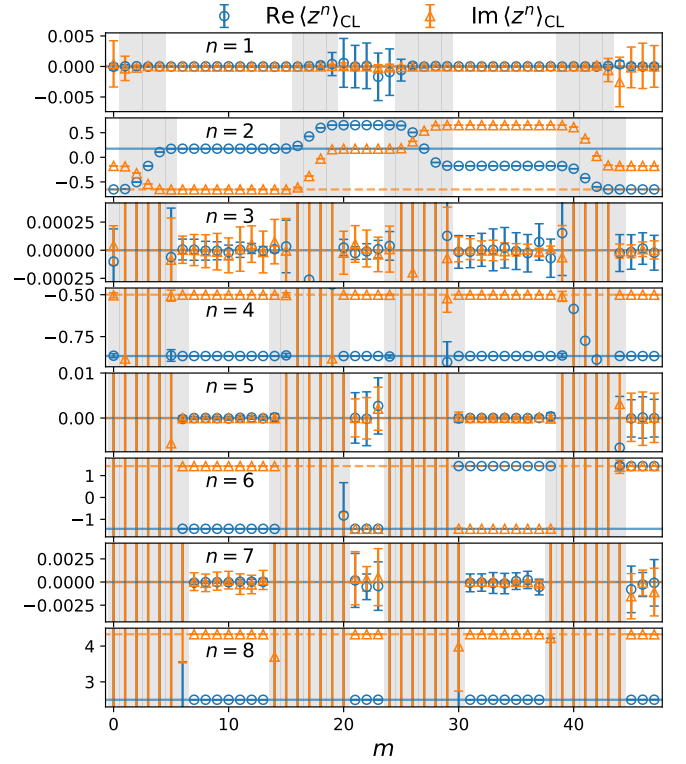


FIG. 5. Real and imaginary parts of the observables  $\langle z^n \rangle_{\text{CL}}$  in the theory (26) with  $l = 5$  in (27) for different  $n$  as a function of the kernel parameter  $m$  in (28). For values of  $m$  within the shaded regions, the corresponding observable has a nonzero boundary term. The solid and dashed horizontal lines indicate the real and imaginary parts of the corresponding exact results (29), respectively.

for this likely has to do with symmetry considerations, as with random initial conditions we find all distributions to be symmetric under the reflection  $z \rightarrow -z$ , under which  $\gamma_1$  and  $\gamma_2$  are invariant (up to inversion), but  $\gamma_3$  changes in a topologically nontrivial way, turning into a different integration cycle.

Generally speaking, there is a certain correlation between the shape of the distribution and the integration cycles that contribute to expectation values. For instance, as we have mentioned, the line sampled for  $m = 10$  is precisely the integration contour used to compute  $\langle z^n \rangle_{\gamma_1}$ . This statement should not be taken at face value, however. Indeed, a distribution that is close (or parallel) to a straight line that lies within the equivalence class of paths described by a certain integration cycle  $\gamma_i$  does not automatically imply that  $\gamma_i$  is the only cycle that contributes. However, it does provide an explanation for the fact that simulations with  $K = 1$ , for which the distributions are approximately parallel to the real line, are plagued by nonzero boundary terms if  $\text{Re } \lambda < 0$ . After all, for this range of  $\lambda$  the real line is not homotopic to any valid integration cycle.

In Fig. 5, we show the observables  $\langle z^n \rangle_{\text{CL}}$  as a function of the kernel parameter  $m$ . Once again, values of  $m$  for

which an observable has a nonzero boundary term are indicated by shaded regions. Many features of Fig. 5 are similar to Figs. 2 and 3, such as the signals for nonvanishing boundary terms becoming clearer (and the presence of boundary terms being correlated with larger uncertainties) for larger values of  $n$ .

The most striking feature of Fig. 5, however, was already observed in [62]. Namely, as was mentioned before, while there are boundary terms and thus simulation results inconsistent with  $\langle z^n \rangle_{\text{exact}}$  for the trivial kernel  $K = 1$  ( $m = 0$ ), a nontrivial kernel can actually ensure that  $\langle z^n \rangle_{\text{CL}} = \langle z^n \rangle_{\text{exact}}$ . This is true especially in the vicinity of  $K = \lambda^{-1/2}$  ( $m = 2l$ ), as anticipated. More precisely, there is a large plateau, of roughly the size 7, around  $m = 10$ , for which the simulation results are compatible with (29). Moreover, there is another such plateau around  $m = 34$ , which plays a similarly special role (see the discussion of Fig. 4), except that it is not associated with  $\langle z^n \rangle_{\text{exact}}$ , and for which boundary terms vanish as well. Finally, there are two more, albeit smaller, plateaus, around  $m = 22$  and  $m = 46$ , respectively. Here, too, boundary terms are consistent with zero but  $\langle z^n \rangle_{\text{CL}} \neq \langle z^n \rangle_{\text{exact}}$  for certain  $n$ . Indeed, as before, for  $n$  either being odd or a multiple of four, the complex Langevin results actually agree with (29) on all plateaus due to the symmetry of those observables. Thus, when we say that simulation results are consistent with (29), what we mean is that  $\langle z^n \rangle_{\text{CL}} = \langle z^n \rangle_{\text{exact}}$  for all  $n$ .

We believe that the fact that there are extended regions in  $m$  (and thus in the kernel  $K$ ) for which boundary terms vanish is a nontrivial finding. Perhaps even more importantly, the observation that simulation results are consistent with the desired values (29) on a large plateau in the kernel parameter could prove valuable for future investigations of more realistic systems using complex Langevin simulations with a nontrivial kernel.

The findings presented so far lead one to expect that the coefficients  $a_i$  in (10) should read  $a_i \approx \delta_{i1}$  in the vicinity of  $m = 10$  but take different values on the other plateaus. To substantiate this claim, we plot the  $a_i$  as a function of  $m$  in Fig. 6. Only points for which a reasonable fit could be obtained are shown. As before, these points correspond to the ones for which boundary terms are consistent with zero. We observe that there are three different scenarios, depending on the kernel parameter  $m$ : First, around  $m = 10$ , the real integration cycle  $\gamma_1$  dominates and contributions from  $\gamma_{i \neq 1}$  are clearly subleading, as expected from Fig. 4. Second, close to  $m = 34$ , it is  $\gamma_2$ , i.e., the imaginary integration cycle, that (almost) exclusively contributes to the complex Langevin results. This, again, can be appreciated from Fig. 4. Finally, on the smaller plateaus around  $m = 22$  and  $m = 46$ , respectively, the simulations sample two different linear combinations of  $\gamma_1$  and  $\gamma_2$ , which, however, is less obvious from Fig. 4. As before, we find the condition (11) to be true and  $a_3$  to be consistent with zero in all of these scenarios. The reason why both the real and imaginary

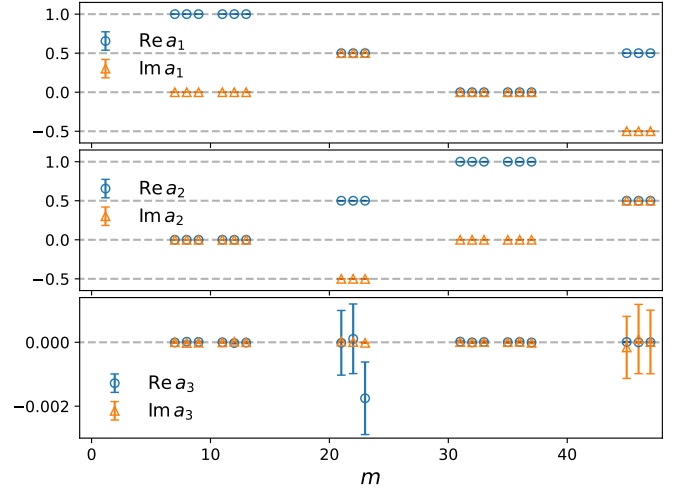


FIG. 6. Real and imaginary parts of the coefficients  $a_i$  in the model (26) with  $\lambda = e^{5i\pi/6}$  as a function of the kernel parameter  $m$  in (28), obtained via the least squares fit procedure outlined in Sec. IV D 3 using the observables (33). We plot only those values of  $m$  for which boundary terms are consistent with zero. The points  $m = 10$  and  $m = 34$ , for which trivially  $a_i = \delta_{i1}$  and  $a_i = \delta_{i2}$ , respectively, are not shown either, as the corresponding coefficients cannot be computed with our approach. The dashed horizontal lines are placed in steps of  $1/2$  to guide the eye.

parts of all coefficients seem to only take values that are multiples of  $1/2$  is not clear to us at this point.

We conclude that the theorem (10) holds in all cases we have investigated so far. While straightforward complex Langevin simulations with  $K = 1$  often suffer from wrong convergence, this can be cured via an appropriate choice of kernel. In particular, we have seen that a kernel of the form (28) can be used to, on the one hand, remove boundary terms and, on the other hand, affect which integration cycles contribute to  $\langle z^n \rangle_{\text{CL}}$ . Hence, in a sense, a kernel can be used to generate rotations in the space of integration cycles. The reason that a kernel as simple as (28) is sufficient to restore correct convergence is owed to the simplicity of the model (26). In more complex models, this might no longer be true and more sophisticated, i.e.,  $z$ -dependent kernels may have to be used. This has been done successfully, e.g., in [66], and we are planning to re-investigate this issue from the point of view of integration cycles in future work. We remark, however, that the existence of a kernel that can ensure correct convergence is – to the best of our knowledge – not guaranteed in general theories.

Up to now, we have mainly provided numerical confirmation for the theorem (10), which was anyways proven to be true in one dimension in [1]. In the next subsection, however, we test its validity when two degrees of freedom are involved. As far as we know, no corresponding proof exists in this case, such that our numerical results are the first hints towards a generalization of (10) to arbitrary dimensions, i.e., arbitrary theories.



## B. Two dimensions

We consider the following class of two-dimensional models:

$$S_a(z_1, z_2) = \frac{\lambda}{4} (z_1^4 + z_2^4 + a z_1^2 z_2^2), \quad (34)$$

where  $z_i \in \mathbb{C}$ ,  $\lambda$  is defined as in (27) and  $a \in \mathbb{R}$  is a tunable parameter controlling the amount of coupling between  $z_1$  and  $z_2$ . In the following, we shall be interested in observables of the form  $\langle z_1^{n_1} z_2^{n_2} \rangle$ , where the  $n_i$  are non-negative integers. As compared to the one-dimensional case, however, for these observables (and  $a \neq 0$ ) there exist no analytical results analogous to (29), such that we have to resort to numerical integration. In the simulations discussed below, we have measured  $\langle z_1^{n_1} z_2^{n_2} \rangle$  for those combinations of  $n_1$  and  $n_2$  with  $n_1 + n_2 \leq 4$ . We shall refer to observables as even if both  $n_1$  and  $n_2$  are even numbers and as odd otherwise. We note that the boundary term expectation values in two dimensions are defined as in (8), with the difference that  $L_c$  is now defined as a sum over degrees of freedom, i.e.,  $L_c = \sum_{i=1}^2 (\partial_i - \partial_i S) K_i \partial_i$ .

We find it adequate at this point to discuss to which extent the two models (26) and (34) can actually be compared with one another. After all, these theories have different numbers of degrees of freedom as well as symmetries. Nevertheless, both actions are polynomials of quartic order with no terms of lower or higher order involved, suggesting that they might at the very least share some common features. Needless to say, this question is highly dependent on the coupling parameter  $a$ :

On the one hand, for  $a = 0$ , the resulting free theory  $S_0$  decomposes into two independent one-dimensional models of the form (26). For complex Langevin simulations with a diagonal kernel, as in our setup, the lack of coupling between  $z_1$  and  $z_2$  means that their respective evolutions are completely decoupled from one another, such that their probability distributions are simply the one-dimensional ones we have already studied (c.f. Fig. 4). This decoupling also makes the discussion of integration cycles particularly simple. Indeed, for  $a = 0$ , one may write the two-dimensional basis integration cycles in terms of the one-dimensional ones as  $\gamma_i \times \gamma_j$ , where the notation indicates that one may integrate over  $z_1$  and  $z_2$  (along  $\gamma_i$  and  $\gamma_j$ , respectively) independently, since the integrals factorize. More precisely, one finds

$$\langle z_1^{n_1} z_2^{n_2} \rangle_{\gamma_i \times \gamma_j} = \langle z_1^{n_1} \rangle_{\gamma_i} \cdot \langle z_2^{n_2} \rangle_{\gamma_j}, \quad (35)$$

where each factor on the right-hand side is a one-dimensional integral of the form (9). Hence, there are  $N_\gamma = 3 \cdot 3 = 9$  independent integration cycles in the theory  $S_0$ . This also means that the entire analysis of Sec. V A carries over directly. For more details on this subject, we refer to Appendix A.

As one varies  $a$  and, thus, introduces a nonzero coupling between  $z_1$  and  $z_2$ , however, these conclusions

might no longer hold. Indeed, for large values of  $a$ , the asymptotics of (34), which determine the possible integration cycles, are no longer governed by the  $z_i^4$  but by the mixing term  $z_1^2 z_2^2$  instead. As is discussed in Appendix A, the dependence of the number of independent integration cycles  $N_\gamma$  on  $a$  has the following peculiar behavior in the model (34):

$$N_\gamma = \begin{cases} 9 & \text{if } |a| < 2, \\ 2 & \text{if } |a| \geq 2. \end{cases} \quad (36)$$

The two points  $a = \pm 2$  are thus special in that they mark the transition from a weak coupling regime, in which the two-dimensional theory bears some resemblance to two independent one-dimensional theories (becoming an equivalence for  $a = 0$ ), to a strong coupling regime in which the interaction term dominates. It is worth emphasizing that the strong-coupling regime is actually simpler than the free theory in terms of the number of relevant integration cycles. We shall now investigate different scenarios, depending on the value of  $a$ , in more detail.

### 1. O(2)-symmetric case

We start by discussing the case  $a = 2$ , i.e., the model

$$S_2(z_1, z_2) = \frac{\lambda}{4} (z_1^2 + z_2^2)^2, \quad (37)$$

which features an O(2) symmetry. In order to define the two linearly independent integration cycles for this model, we introduce two variables  $\xi_1$  and  $\xi_2$  in analogy to (30). Then, as before, we define  $\gamma_1$  to be the real integration cycle in these new variables. More precisely,  $\gamma_1$  is the equivalence class of integration surfaces that are homotopic to the two-dimensional real submanifold of  $\mathbb{C}^2 \ni (\xi_1, \xi_2)$ . Similarly, we define  $\gamma_2$  to be the corresponding imaginary cycle. In the notation of Eq. (35), these two basis cycles may be represented as  $\gamma_1 \times \gamma_1$  and  $\gamma_2 \times \gamma_2$ , respectively, where we use the same symbol for the one- and two-dimensional cycles. As before, we define  $\langle z_1^{n_1} z_2^{n_2} \rangle_{\text{exact}} := \langle z_1^{n_1} z_2^{n_2} \rangle_{\gamma_1}$ , but emphasize once again that this is merely a choice; the result of the  $\gamma_1$ -integration is by no means more correct than the one over  $\gamma_2$ .

Given the success of our analysis in the one-dimensional model (26), we now essentially repeat the steps of Sec. V A for the theory (37). To begin with, we employ a trivial kernel,  $K_1 = K_2 = 1$ , in (16). Moreover, we once again introduce the difference

$$\Delta^{(n_1, n_2)} := \langle z_1^{n_1} z_2^{n_2} \rangle_{\text{CL}} - \langle z_1^{n_1} z_2^{n_2} \rangle_{\text{exact}} \quad (38)$$

to quantify the deviations between complex Langevin and exact results. As a two-dimensional analog of Fig. 2, we plot  $\Delta^{(n_1, n_2)}$  as a function of the parameter  $l$  in (27) for the even observables in Fig. 7. Most of the conclusions drawn in the context of Fig. 2 also hold true in the



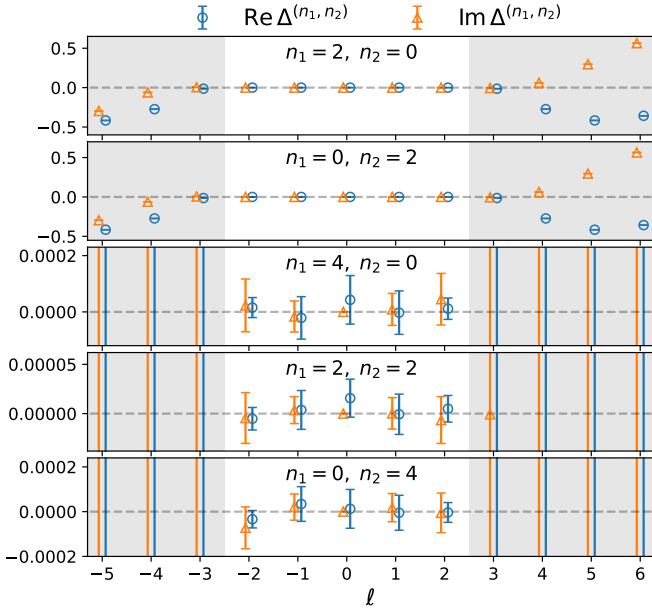


FIG. 7. Similar as in Fig. 2 but for  $\Delta^{(n_1, n_2)}$ , as defined in (38), and in the model (37).

present case, such that we refrain from repeating them. Note, however, that, while there were no boundary terms for  $l = 6$  in the one-dimensional case, this is no longer true in the model (37). This has to do with the way two-dimensional integration cycles are related to their one-dimensional counterparts and shall be discussed in more detail below. As a consequence, we find agreement between simulation and exact results for all values of  $\lambda$  without boundary terms. We do not show the odd observables here, as we find them all to be consistent with zero whenever boundary terms vanish. Under the assumption that (10) indeed holds in two dimensions, this is not surprising, given that  $\langle z_1^{n_1} z_2^{n_2} \rangle_{\gamma_1} = \langle z_1^{n_1} z_2^{n_2} \rangle_{\gamma_2} = 0$  if at least one of  $n_1$  and  $n_2$  is odd.

The latter fact also implies that we have to restrict to the even observables for the computation of the coefficients  $a_i$  in (10). Thus, we choose the following set of observables, being the largest one possible, for the least-squares fit:

$$\{\langle z_1^2 \rangle, \langle z_2^2 \rangle, \langle z_1^4 \rangle, \langle z_1^2 z_2^2 \rangle, \langle z_2^4 \rangle\}. \quad (39)$$

With this and  $N_\gamma = 2$ , we proceed as before in order to compute the  $a_i$  and we show their  $l$ -dependence in Fig. 8. We find  $a_1 \approx 1$  and  $a_2 \approx 0$  for all  $\lambda$  with vanishing boundary terms, while the fits become unstable when boundary terms are nonzero. This is a nontrivial finding and a first hint of the validity of (10) beyond one dimension. It is also noteworthy that we do not observe any nontrivial linear combinations of  $\gamma_1$  and  $\gamma_2$  here, even though they would be allowed according to (10). While, as we have mentioned, one may not easily establish a direct connection between the models (26) and (37), we nonetheless conclude that one may encounter situations

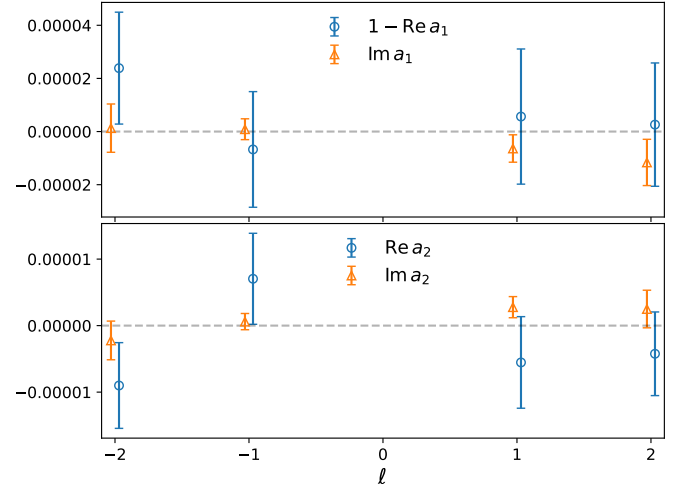


FIG. 8. Real and imaginary parts of the coefficients  $a_i$  in the model (37) as a function of the parameter  $l$  in (27), obtained via the least-squares fit procedure outlined in Sec. IV D 3 using the observables (39). We only plot those values of  $l \neq 0$  for which boundary terms are consistent with zero. The point  $l = 0$ , for which  $a_i = \delta_{i1}$ , trivially, is not shown either as the corresponding coefficients cannot be computed with our approach. The dashed horizontal lines indicate zero. Note that the upper panel shows  $1 - \text{Re } a_1$  and the data points have been displaced horizontally, both for reasons of readability.

where the analysis of integration cycles simplifies rather dramatically when increasing the number of degrees of freedom.

As in one dimension, complex Langevin simulations of (37) with a trivial kernel cannot reproduce the exact results for most values of  $\lambda$ , in particular those with  $\text{Re } \lambda < 0$ , due to the presence of boundary terms. In an attempt to nonetheless obtain an answer for these values, we thus once again introduce a nontrivial kernel and consider  $l = 5$  in (27) as a representative. While, in principle, we may choose  $K_1 \neq K_2$  in (16), we instead take both kernel elements to be equal for the time being. This implies that  $z_1$  and  $z_2$  are being treated on completely equal footing, which must be reflected in their respective distributions coinciding. Moreover, we parametrize  $K := K_1 = K_2$  as in (28), using an integer  $m$ .

The effect of this choice of kernel on the probability distributions is shown in Fig. 9, which is an analog of Fig. 4 for the two-dimensional model (37). Since we have verified that the distributions are indeed identical for  $z_1$  and  $z_2$ , we only show those of the former. The general features of the two-dimensional distributions closely resemble those discussed in Fig. 4. In particular, for  $m = 10$  and  $m = 34$ , the distributions are again confined to lines, such that we expect values of  $m$  close to 10 to give the best agreement with  $\langle z_1^{n_1} z_2^{n_2} \rangle_{\text{exact}}$  due to our definition of  $\gamma_1$ . There is one major difference between Figs. 4 and 9, however. Namely, in the latter we do not observe an ergodicity problem anymore, as the two high-probability regions are now connected to each other. This means that

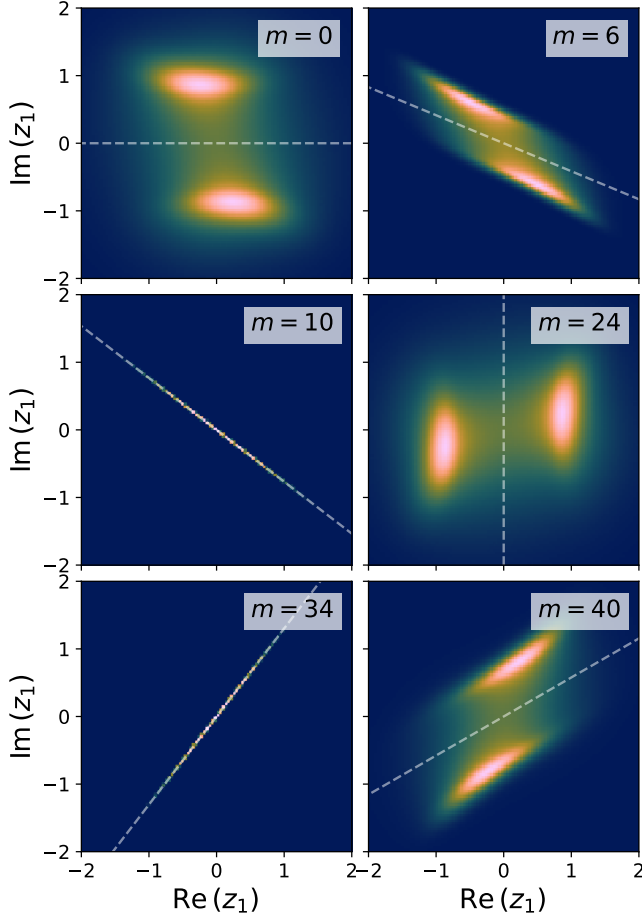


FIG. 9. Histograms of  $z_1$  obtained in complex Langevin simulations of the model (37) with  $\lambda = e^{5i\pi/6}$  and different kernels  $K = e^{-mi\pi/24}$ , chosen equal for both variables. The brighter regions indicate a higher probability and the dashed lines lie in the direction of the argument of the noise coefficients  $\sqrt{K}$ . The respective histograms of  $z_2$  are identical and thus not shown.

the strong interaction between  $z_1$  and  $z_2$  allows each of them to transition between the high-probability regions, which would not be possible for  $a = 0$ .

The  $m$ -dependence of the even observables is shown in Fig. 10. As before, we once again observe large plateaus in the vicinity of  $m = 10$  and  $m = 34$ , respectively. In fact, these plateaus appear to be slightly larger than those in Fig. 5. However, contrary to the one-dimensional case, the additional plateaus near  $m = 22$  and  $m = 46$  are absent here and instead one finds boundary terms for those values. We interpret this finding as follows: as we have mentioned, in one dimension, a single simulation with  $m$  close to 22 or 46 may sample  $\gamma_3$  due to the ergodicity problem, even though its contributions cancel in the average over simulations. Something similar would happen in the model (34) for small values of  $a$ , for which appropriate extensions of  $\gamma_3$  to two dimensions still constitute valid integration cycles. For  $a = 2$ , however, this is no longer true, implying that such a choice

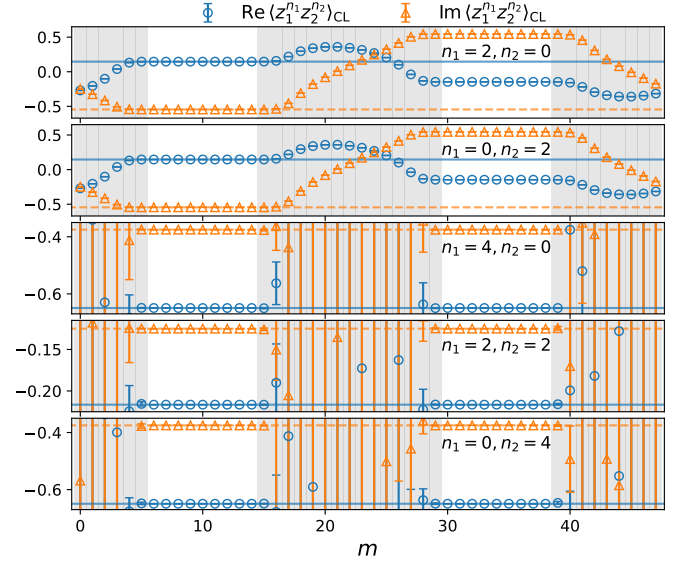


FIG. 10. As in Fig. 5 but for the observables  $\langle z_1^{n_1} z_2^{n_2} \rangle_{\text{CL}}$ , with  $n_1$  and  $n_2$  both even, in the theory (37), using  $K_1 = K_2$ , both parametrized in terms of the integer  $m$  in (28).

of kernel forces the system onto a kind of unstable trajectory, resulting in nonzero boundary terms. This is also the reason why there are boundary terms for  $l = 6$  in Fig. 7, while they are absent in Figs. 2 and 3. Once again, we refrain from plotting the odd observables, as they are trivial.

In Fig. 11, we show fits for the two coefficients  $a_1$  and  $a_2$  as a function of  $m$ . As expected from the previous discussion, we find that  $\gamma_1$  dominates on the plateau around  $m = 10$ , while  $\gamma_2$  becomes dominant in the vicinity of  $m = 34$ . As for  $K_i = 1$ , we once again do not observe any nontrivial linear combinations involving both  $\gamma_1$  and  $\gamma_2$ . Moreover, as in all previous cases, we obtain stable fits if and only if boundary terms are absent, which makes another strong point for the validity of (10) in general theories. Once again, the dramatic effect that different choices of kernel can have on the coefficients  $a_i$  can hardly be overemphasized.

## 2. General couplings

We have seen before that the class of models (34) behaves in a qualitatively different way depending on whether  $a$  is smaller or larger than two, since the number of independent integration cycles jumps from 9 to 2 at that value according to (36). As the final analysis of this work, we shall devote this subsection to a discussion of how this transition is reflected on the level of complex Langevin simulations by studying distributions of  $z_1$  and  $z_2$  for different values of  $a$ .

In the following, we once again consider  $\lambda = e^{5i\pi/6}$  in (34), i.e.,  $l = 5$  in (27). Now, however, we allow the two kernel elements  $K_1$  and  $K_2$  to vary independently

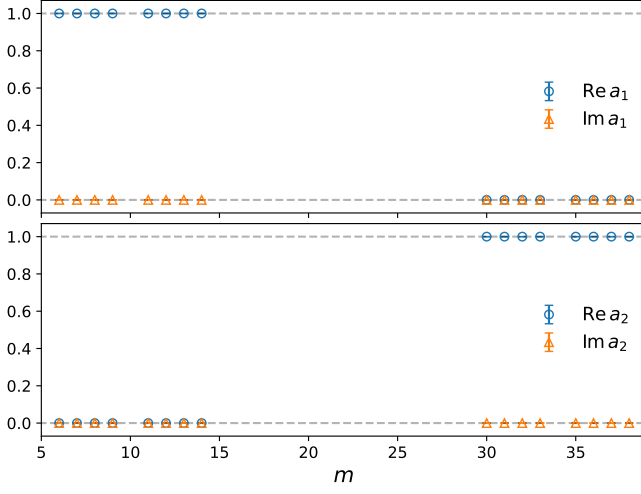


FIG. 11. Analogous to Fig. 6 but for the model (37) with  $\lambda = e^{5i\pi/6}$  and using  $K_1 = K_2$ , each parametrized by the integer  $m$  in (28). For the least-squares fit we have used the observables (39) and  $N_\gamma = 2$ . The dashed horizontal lines at 0 and 1 are there to guide the eye.

of each other. To this end, we introduce two integers  $m_1$  and  $m_2$ , parametrizing  $K_1$  and  $K_2$  as in (28), respectively, but restrict them to the values  $m_i \in \{10, 22, 34\}$ . For  $a < 2$ , this should allow us to probe a large variety of different integration cycles. In particular, for  $a = 0$  we have seen that the two-dimensional integration cycles trivially result from combinations of two independent one-dimensional ones. Since in one dimension we have seen that we can generate contributions from  $\gamma_1$  and  $\gamma_2$  rather easily, we expect to be able to sample at least four different two-dimensional cycles for small values of  $a$ . We note that it is not our primary concern in this investigation to obtain simulation results that match  $\langle z_1^{n_1} z_2^{n_2} \rangle_{\text{exact}} := \langle z_1^{n_1} z_2^{n_2} \rangle_{\gamma_1}$ . After all, we know that this can be achieved with the choice  $K_1 = K_2 = \lambda^{-1/2}$ . Rather, we aim at obtaining a better understanding of how exactly the simulation trajectories are affected by nontrivial kernels and how this may influence the sampling of different integration cycles.

Our choice of parametrizing  $K_1$  and  $K_2$  individually implies that the respective distributions of  $z_1$  and  $z_2$  need no longer be equivalent in general. A trivial example is given by  $a = 0$ , for which the respective distributions of  $z_1$  and  $z_2$  are simply those shown in Fig. 4 (with  $m$  replaced by  $m_1$  and  $m_2$ , respectively). Introducing a small coupling  $a \neq 0$  should then cause these distributions to wash out to a certain degree. This effect is seen in the center panel of Fig. 12, in which we show histograms of  $z_1$  and  $z_2$  that result from different combinations of  $m_1$  and  $m_2$  at an intermediate interaction strength  $a = 1$ . Observe, however, that no such distortion occurs if both  $m_i \in \{10, 34\}$ . For these particular choices of kernel, both distributions remain confined to their respective lines despite the interaction. We em-

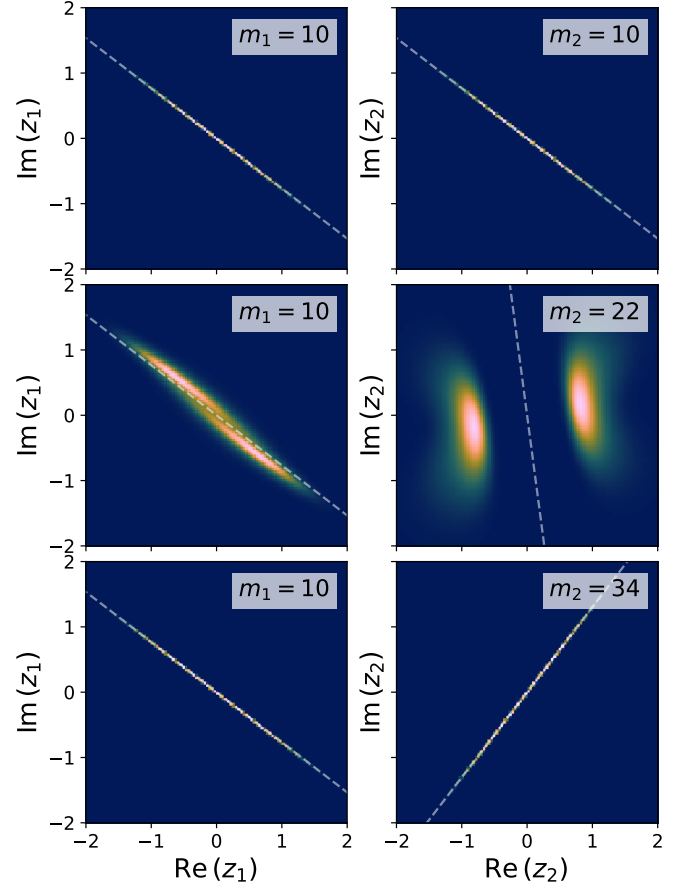


FIG. 12. Histograms of  $z_1$  (left column) and  $z_2$  (right column) obtained in complex Langevin simulations of the model (34) with  $\lambda = e^{5i\pi/6}$  and  $a = 1$ . The kernel elements  $K_1$  and  $K_2$  are parametrized as in (28) using integers  $m_1$  and  $m_2$ , respectively. The top, center and bottom rows correspond to  $(m_1, m_2) = (10, 10)$ ,  $(10, 22)$ , and  $(10, 34)$ , respectively. The brighter regions indicate a higher probability and the dashed lines lie in the directions of the arguments of the respective noise coefficients  $\sqrt{K_i}$ .

phasize that this does not imply that the trajectories of  $z_1$  and  $z_2$  are independent of one another. On the contrary, their correlations increase with  $a$  irrespectively of the one-dimensional confinement.

For the case  $m_1 = m_2 = 22$ , we show the histograms of  $z_1$  and  $z_2$  for different values of  $a$  in Fig. 13. One clearly observes how increasing the interaction strength induces a higher transition probability between the two high-probability regions. This even results in the curious observation that for the super-critical coupling  $a = 3.000$  there appear to be three instead of two high-probability regions, all of which are parallel to  $\sqrt{K_i}$ . Note, however, that there is no significant change in the distributions in the vicinity of  $a = 2$ .

At this point, we mention a peculiarity we have observed in our simulations: To begin with, we have performed simulations for values of  $a$  equal to 0, 0.5, 1, 1.5, 1.99, 2, and 3, supplemented by a few smaller ensembles

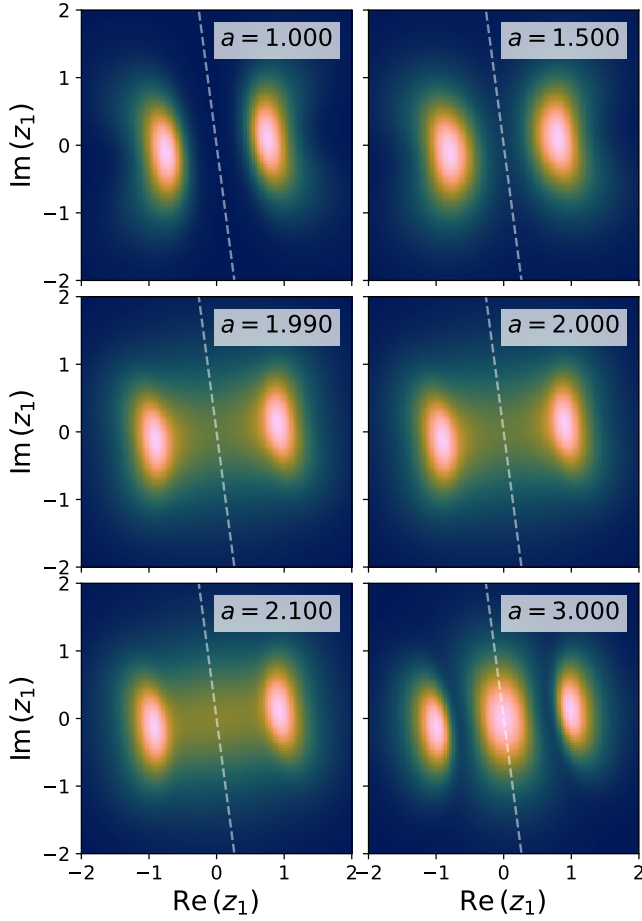


FIG. 13. Histograms of  $z_1$  obtained in complex Langevin simulations of the model (34) with  $\lambda = e^{5i\pi/6}$  and different values of the coupling parameter  $a$ . We use equal kernels  $K_1 = K_2$ , defined as in (28), with  $m_i = 22$ , such that the respective distributions of  $z_2$  are identical. The brighter regions indicate a higher probability and the dashed lines lie in the direction of the argument of the noise coefficients  $\sqrt{K_i}$ .

at  $a = 0.1, 1.9$  and  $2.1$ , and considered all possible combinations of  $m_i \in \{10, 22, 34\}$  for each of them. Now, for all  $a < 2$ , there were no major issues in any of the runs. As soon as we crossed the critical point  $a = 2$ , however, we encountered problems that were not present before. In particular, for  $a = 2$ , the simulations with  $m_1 = 22 \neq m_2$  or *vice versa* slowed down drastically, preventing the algorithm from generating an ensemble of suitable size to perform averages over. This is likely caused by the adaptive step size algorithm producing smaller and smaller  $\varepsilon$  due to the drift terms blowing up. It also makes clear that one may not use arbitrary kernels for arbitrary theory parameters and still obtain viable results. The failure of simulations for these particular combinations of  $m_1$  and  $m_2$  seems to be specific to  $a = 2$ , however. For  $a = 2.1$  and  $a = 3$ , on the other hand, we do not obtain results only when  $m_1 = 10, m_2 = 34$  or *vice versa*.

To put the results discussed so far into context, we show in Fig. 14 the observable  $\langle z_1^2 \rangle_{\text{CL}}$  for various values

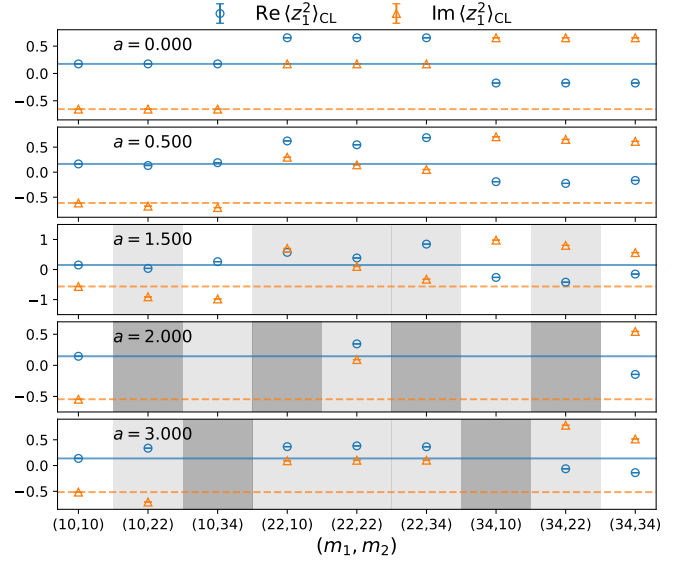


FIG. 14. Real and imaginary parts of the observable  $\langle z_1^2 \rangle_{\text{CL}}$  in the theory (34) with  $l = 5$  in (27) for different values of  $a$ . The horizontal axis corresponds to different combinations of the integers  $m_1$  and  $m_2$ , parametrizing the kernel elements  $K_1$  and  $K_2$  as in (28), respectively. For combinations  $(m_1, m_2)$  within the light shaded regions, there are nonzero boundary terms for  $\langle z_1^2 \rangle_{\text{CL}}$  and the dark shaded regions indicate those  $(m_1, m_2)$  and  $a$  for which no simulation results could be obtained. The solid and dashed horizontal lines indicate the real and imaginary parts of the corresponding exact results, respectively, and the axis limits have been chosen such that all results without boundary terms are fully visible.

of  $a$  and different combinations of  $m_1$  and  $m_2$ . Those parameters for which we could not obtain results via simulations are marked by the dark shaded regions. Once again, we observe that while the presence of boundary terms indicates that  $\langle z_1^{n_1} z_2^{n_2} \rangle_{\text{CL}} \neq \langle z_1^{n_1} z_2^{n_2} \rangle_{\text{exact}}$ , the converse is not true, as some simulation results are seen to deviate from the exact ones despite boundary terms being consistent with zero. Other observables look qualitatively similar and are hence not shown here.

In Fig. 14, we trivially observe that there are no boundary terms in the free theory  $a = 0$  when the  $m_i$  only take the values 10, 22, or 34. This simply reflects the results of Fig. 5, since for  $a = 0$  we are simulating two independent one-dimensional theories of the form (26). As one increases  $a$ , however, the interaction between  $z_1$  and  $z_2$  starts to become relevant, which has a nontrivial effect on the asymptotics of  $S_a$  and, by extension, affects which contours are valid integration cycles. In turn, this has an influence on which trajectories, governed by the choice of  $m_1$  and  $m_2$ , produce boundary terms. As seen in Fig. 14, for  $a \lesssim 2$ , only kernels with  $m_i \in \{10, 34\}$  cause boundary terms to vanish and we observe the onset of this behavior around  $a \approx 1$ . At and beyond the critical point  $a = 2$ , we are then confronted with the situation that certain kernels do not produce usable results at all. Now, only the choices



$(m_1, m_2) = (10, 10)$  and  $(34, 34)$  ensure simulations free of boundary terms. We expect these results not to change significantly when the kernel parameters  $m_i$  are varied slightly, i.e., there should be plateaus in both  $m_1$  and  $m_2$  on which boundary terms vanish. In particular, we expect there to be a plateau around  $(m_1, m_2) = (10, 10)$ , on which  $\langle z_1^{n_1} z_2^{n_2} \rangle_{\text{CL}} = \langle z_1^{n_1} z_2^{n_2} \rangle_{\text{exact}}$ .

Finally, we study how these choices of kernel affect the coefficients  $a_i$  in (10). We begin with the simpler case  $a \geq 2$ . In this case, as we have seen before, there are only  $N_\gamma = 2$  integration cycles, namely the real and imaginary cycles  $\gamma_1$  and  $\gamma_2$ , respectively. From Fig. 11, we know that we may sample the former with choices of  $(m_1, m_2)$  close to  $(10, 10)$  and the latter with kernel parameters around  $(34, 34)$ . On the other hand, for the combinations with  $m_1 \neq m_2$  that we have studied, as well as for the choice  $m_1 = m_2 = 22$ , we do not obtain stable fit results, as in these cases we either find nonzero boundary terms or no results at all.

The case  $a < 2$  is less straightforward. First of all, since we now have to take into account  $N_\gamma = 9$  independent integration cycles, the set of five even observables (39) is no longer sufficient to obtain a reasonable fit. Instead, we include all the observables we have measured, i.e., all  $\langle z_1^{n_1} z_2^{n_2} \rangle_{\text{CL}}$  with  $n_1 + n_2 \leq 4$ . Next, we need to define a suitable basis set of integration cycles. For  $a = 0$ , in particular, we have seen above that one possible basis set consisting of nine cycles is given by the product  $\gamma_i \times \gamma_j$ , where  $\gamma_i$  and  $\gamma_j$  are one-dimensional cycles. In particular, we define

$$\begin{aligned} \gamma_1 &:= \gamma_1 \times \gamma_1, & \gamma_2 &:= \gamma_2 \times \gamma_2, & \gamma_3 &:= \gamma_1 \times \gamma_2, \\ \gamma_4 &:= \gamma_2 \times \gamma_1, & \gamma_5 &:= \gamma_1 \times \gamma_3, & \gamma_6 &:= \gamma_3 \times \gamma_1, \\ \gamma_7 &:= \gamma_2 \times \gamma_3, & \gamma_8 &:= \gamma_3 \times \gamma_2, & \gamma_9 &:= \gamma_3 \times \gamma_3. \end{aligned} \quad (40)$$

Note that each of these cycles is really an equivalence class of integration surfaces in  $\mathbb{C}^2$ . Now, as is outlined in Appendix A, most of these equivalence classes shrink in size as  $a$  increases. However, one may nonetheless find certain representatives within them that constitute valid integration cycles for all  $|a| < 2$ , such as the ones we use to compute  $\langle z_1^{n_1} z_2^{n_2} \rangle_{\gamma_i}$ . Thus, in a slight abuse of notation, we shall consider the same basis (40) for all  $|a| < 2$ , keeping in mind that one should restrict to certain subclasses of integration surfaces in practice. With this, we now compute the  $a_i$  for values of the coupling  $a < 2$ .

We mention that in the cases where at least one of the distributions of  $z_1$  or  $z_2$  is confined to a line, our fitting procedure cannot be applied due to the covariance matrix  $\Sigma$  in (25) being singular. In these cases, however, the relevant integration cycles are anyways easy to guess and the theorem (10) holds trivially. For  $a = 0$ , this excludes all combinations  $(m_1, m_2)$  except  $(22, 22)$  for the fit. For this kernel, we find that

$$a_1 \approx \frac{i}{2}, \quad a_2 \approx -\frac{i}{2}, \quad a_3 \approx \frac{1}{2}, \quad a_4 = \frac{1}{2} \quad (41)$$

within errors, whereas  $a_{i>4} \approx 0$ , all in agreement with (11). This is precisely the combination of coefficients one

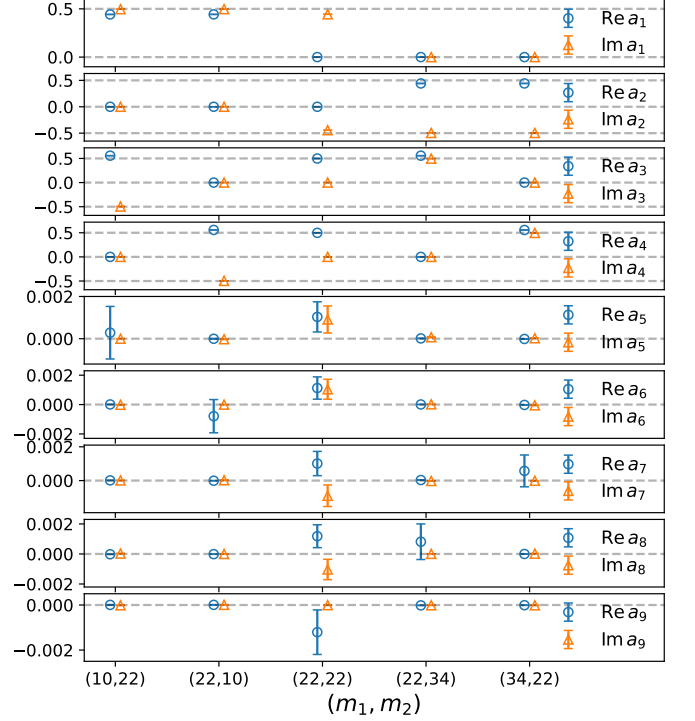


FIG. 15. Real and imaginary parts of the coefficients  $a_i$  in the model (34) with  $\lambda = e^{5i\pi/6}$  and  $a = 0.5$ , obtained via the least-squares fit procedure outlined in Sec. IV D 3 using the observables  $\langle z_1^{n_1} z_2^{n_2} \rangle$  with  $n_1 + n_2 \leq 4$ . The horizontal axis corresponds to different combinations of the integers  $m_1$  and  $m_2$ , where we only show those combinations for which the distribution of neither  $z_1$  nor  $z_2$  is confined to a line. The dashed horizontal lines are placed in steps of  $1/2$  to guide the eye and the data points have been displaced horizontally for better visibility. Note that there are no boundary terms for any of the  $(m_1, m_2)$  shown.

would have expected based on the results of Fig. 6. Also note that once more the real and imaginary parts of all coefficients are integer multiples of  $1/2$ .

Since in our one-dimensional simulations with a kernel of the form (28) we could not sample  $\gamma_3$ , one is led to expect that with our choice of two-dimensional kernel, the linear combinations of cycles on the right-hand side of (10) are likely restricted to  $i \leq 4$  for all  $|a| < 2$ , as they are for  $a = 0$ . What is more, the only kernel for which we expect to sample all four of these integration cycles is precisely the one given by  $(m_1, m_2) = (22, 22)$ . For the other combinations of  $m_1$  and  $m_2$ , at most two out of these four cycles should contribute. To substantiate this claim, we next investigate the case  $a = 0.5$ . Owing to the smallness of the coupling, matters should still be qualitatively similar to the free theory. Now, however, since the distributions of  $z_1$  and  $z_2$  are confined to lines only if both  $m_i \in \{10, 34\}$ , c.f., Fig. 12, we may fit the  $a_i$  for a larger set of kernels.

We plot the coefficients for  $a = 0.5$  and different kernel parameters  $(m_1, m_2)$  in Fig. 15. Indeed, we find four in-



tegration cycles to be relevant when  $(m_1, m_2) = (22, 22)$  and two otherwise. For no choice of kernel do we find  $\gamma_{i>4}$  to contribute significantly. We remark, however, that this might no longer be true when considering more complicated kernels, such as full matrix kernels or kernels depending on the  $z_i$  explicitly. We are unable to perform an analogous analysis for the cases  $a = 1$  and  $a = 1.5$ , as there are nonvanishing boundary terms whenever at least one of the  $m_i$  is equal to 22, while the covariance matrices are singular in all other cases. Finally, we note that, even though it is not easy to see in Fig. 15 for nonzero couplings the real and imaginary parts of the coefficients are actually no longer restricted to being multiples of  $1/2$ , but start to deviate slightly.

## VI. SUMMARY AND CONCLUSIONS

We have investigated the problem of wrong convergence in complex Langevin simulations. In particular, we have studied the toy models (26) and (34) using various different kernels  $K$  in the complex Langevin equation (4). We found that, on the one hand, an appropriate choice of kernel can affect the distributions of the dynamical degrees of freedom in the complex plane in such a way that the measured monomial observables have vanishing boundary terms, a commonly employed correctness criterion in the complex Langevin approach. On the other hand, however, we have also shown that in some simulations without boundary terms the observables are still spoiled by unwanted integration cycles, in accordance with the theorem (10).

We found that (10) holds in all our one- and two-dimensional simulations, indicating that there might be a straightforward extension of the proof of the theorem in [1] to higher, and likely arbitrary, dimensions. We emphasize that contributions from unwanted integration cycles appear most prominently when a nontrivial kernel is used. In particular, our findings substantiate the claim that such spurious solutions to the complex Langevin equation should become relevant only in the presence of a nontrivial kernel or if the density  $e^{-S}$  has singularities in the vicinity of the real axis [37].

As the second major result of this work, we have demonstrated how a kernel can be used – in principle – to control which integration cycles are sampled in a simulation. In particular, due to the deformation of distributions caused by nontrivial kernels, different cycles might be sampled for different arguments of  $K$ . Importantly, however, the introduction of a kernel may also make things worse in a sense. For instance, depending on the parameters of a theory, a kernel might force the simulation trajectories onto shapes which are not homotopic to any integration cycles of the theory. We have found evidence for this scenario to give rise to nonvanishing boundary terms. Even more importantly, the absence of boundary terms in the presence of a kernel does not guarantee correct results. While we have found

large plateaus around the ‘perfect’ choice of kernel on which the desired values of observables are reproduced, there are equally large plateaus with vanishing boundary terms for which one finds different results.

At the moment, it is not clear to us to which extent our results can be generalized to more realistic theories, such as lattice models or even gauge theories. While one might expect the complexity (and the number) of integration cycles to increase the more degrees of freedom are involved, which would make an analysis like the one presented here impossible, we have also discussed a counterexample in this work. Namely, in the strong-coupling ( $a \geq 2$ ) regime of the two-dimensional model (34), the analysis of integration cycles, in fact, becomes more straightforward than in the one-dimensional counterpart (26). One can only speculate whether strongly coupled lattice theories with complicated interaction terms could actually feature a tractable number of integration cycles or one might even find  $N_\gamma = 1$ . If the latter is not true, however, then any attempt of solving quantum field theories by means of the complex Langevin approach with a nontrivial kernel runs the risk of sampling unwanted integration cycles. We believe that this is something one should be aware of. In particular, it might be relevant for approaches in which one attempts to find suitable kernels by the means of machine learning [48, 50].

We plan to investigate this issue in more detail in future work. In particular, we have obtained preliminary results in a model similar to (26) but with multiple interaction terms, for which a  $z$ -independent kernel is no longer sufficient, but a  $z$ -dependent kernel producing correct results can nonetheless be found rather easily [66]. Our results suggest that the findings presented here can be extended to that case rather straightforwardly. Notice, however, that in such simple theories it is possible to essentially guess what form an appropriate kernel should have. This, however, is far from straightforward in more general theories.

Another interesting research question is to study the connection between the sampling of unwanted integration cycles and the spectral properties of the underlying Fokker–Planck operator [41, 49]. In particular, in [49] correct results in a model similar to the ones studied in this work were associated with boundary terms being absent and the Fokker–Planck operator having only eigenvalues with a negative real part.

## ACKNOWLEDGMENTS

We express our gratitude towards Enno Carstensen and Ion-Olimpiu Stamatescu for valuable discussions on a regular basis and for fruitful collaborations past and present. The numerical results presented in this work have been obtained in part in simulations on the computing cluster of the University of Graz (GSC) and the Vienna Scientific Cluster (VSC). This research was funded in part by the Austrian Science Fund (FWF) via the

Principal Investigator Project [P36875](#). The analyses performed in this work are based on the `Python` ecosystem for scientific computing [\[67\]](#), explicitly through the use of the packages [\[68–72\]](#), but we are also grateful for the creation and maintenance of all their dependencies. Moreover, the numerical integrations were computed with the help of the `Wolfram Mathematica` software system [\[73\]](#).

## OPEN ACCESS STATEMENT

For the purpose of open access, the authors have applied a Creative Commons Attribution (CC BY) license to any author-accepted manuscript version arising.

## DATA AVAILABILITY STATEMENT

The full data set underlying this work is available under [\[56\]](#) and the analysis scripts used are published online as well [\[57\]](#). Moreover, our simulation code is available upon request.

## Appendix A: Counting integration cycles

Contrary to the one-dimensional case discussed in Sec. [IIIB](#), the counting of linearly independent integration cycles is nontrivial when two or more degrees of freedom are involved. This is due to the fact that there is no analog as simple as [\(13\)](#) for the addition of two  $d$ -dimensional integrals. We thus devote this Appendix to developing a counting algorithm for integration cycles in arbitrary dimensions. However, we restrict ourselves to theories with regular actions  $S$ , which precludes the existence of closed-loop integration cycles. All theories with polynomial actions, for instance, are of this type. For a different approach of counting independent integration cycles, see [\[52\]](#).

Let us consider a theory with  $d$  complex degrees of freedom  $z_i$ . In order to define integration cycles for such theories, we develop an intuitive language, which might not be the most elegant from a mathematical point of view, but which avoids the introduction of some rather advanced concepts of algebraic topology. The key point to note is that an integration cycle is a  $d$ -dimensional submanifold of the  $2d$ -dimensional space  $\mathbb{C}^d$ , with the important property that  $e^{-S}$  vanishes on its boundaries. Since we consider only regular actions, those boundaries necessarily lie at complex infinity. More precisely, an integration cycle is actually an equivalence class of such manifolds, the equivalence relation being that they share the same boundary conditions. For all practical purposes, however, it is sufficient to consider only one representative out of each equivalence class and this shall be the goal in what follows. In particular, we aim at finding the simplest such representatives possible.

To this end, we consider the subclass of integration manifolds within each equivalence class described by a  $d$ -dimensional cycle  $\gamma$  that can be written as  $d$  independent contour integrals, i.e.,

$$\int_{\gamma} d^d z = \int_{a_i}^{b_i} dz_1 \int_{a_2}^{b_2} dz_2 \cdots \int_{a_d}^{b_d} dz_d =: \int_a^b d^d z. \quad (\text{A1})$$

Here, the  $\int_{a_i}^{b_i} dz_i$  are, with a slight abuse of notation, defined to be integrals along arbitrary one-dimensional contours connecting the points  $a_i$  and  $b_i$  and we have introduced the right-hand side of [\(A1\)](#) as a shorthand notation, with  $a_i$  being the components of  $a$  and similar for  $b$ . Needless to say, in order for  $\gamma$  to constitute a valid integration cycle in a theory with an action  $S$ , the integral [\(A1\)](#) with the integrand  $e^{-S}$  must exist. A necessary condition for this is that the points  $a$  and  $b$  both lie in regions at complex infinity in which  $e^{-S}$  vanishes. To be more concrete, let us introduce polar coordinates,  $z_i = r_i e^{i\theta_i}$ , as in Sec. [IIIB](#) and define  $r^2 := \sum_{i=1}^d r_i^2$ . We can then again identify disjoint regions  $G_i$  in the space spanned by the  $\theta_i$  (with periodic boundary conditions), i.e., the torus  $\Theta_d := [0, 2\pi)^d$ , in which  $e^{-S} \rightarrow 0$  as  $r \rightarrow \infty$ . Let us define the tuple of complex arguments of  $z$  as  $\arg z := (\arg z_1, \dots, \arg z_d)$ . Then, in light of [\(A1\)](#), we require that  $\arg a \in G_i$  while  $\arg b \in G_j$  with  $i \neq j$ , and that  $\sum_{i=1}^d |a_i|^2 = \infty$  and analogously for  $b$ .

Although this is a necessary condition for [\(A1\)](#) to exist, it is not a sufficient one. To see this, consider exchanging any of the  $a_i$  with the corresponding  $b_i$ , resulting in a sign flip of the integral [\(A1\)](#), i.e.,

$$\int_{a_1}^{b_1} dz_1 \cdots \int_{b_i}^{a_i} dz_i \cdots \int_{a_d}^{b_d} dz_d = - \int_a^b d^d z. \quad (\text{A2})$$

Obviously, if the integral on the right should exist, then so must the one on the left. This, however, has to be true for any number of exchanges between the upper and lower limits in the integral, as it changes the result at most by a sign. This imposes severe restrictions on the possible  $a$  and  $b$  that give rise to valid integration cycles. More concretely, let us define the set of points whose  $i$ -th coordinates are either  $a_i$  or  $b_i$ ,

$$X := \{(x_1, x_2, \dots, x_d) \mid x_i \in \{a_i, b_i\}\}. \quad (\text{A3})$$

Then, what is required for  $\int_a^b d^d z$  to define a valid representative of a cycle  $\gamma$  is that the tuples  $\arg x$  for the different  $x \in X$  all lie in different regions  $G_i$ .

In the following, we shall develop a graphical interpretation of this picture that is based on rectangular cuboids in the space  $\Theta_d$ , namely those cuboids whose vertices are given by  $\arg x$  for  $x \in X$  and whose sides are thus parallel to the coordinate axes. Indeed, since the regions  $G_i$  are disjoint subsets of  $\Theta_d$ , a sufficient requirement for the integral  $\int_a^b d^d z$  to represent an integration cycle is that the vertices of the cuboid defined by  $X$  are each contained in a different  $G_i$ . Note that  $\arg a$  and  $\arg b$  are

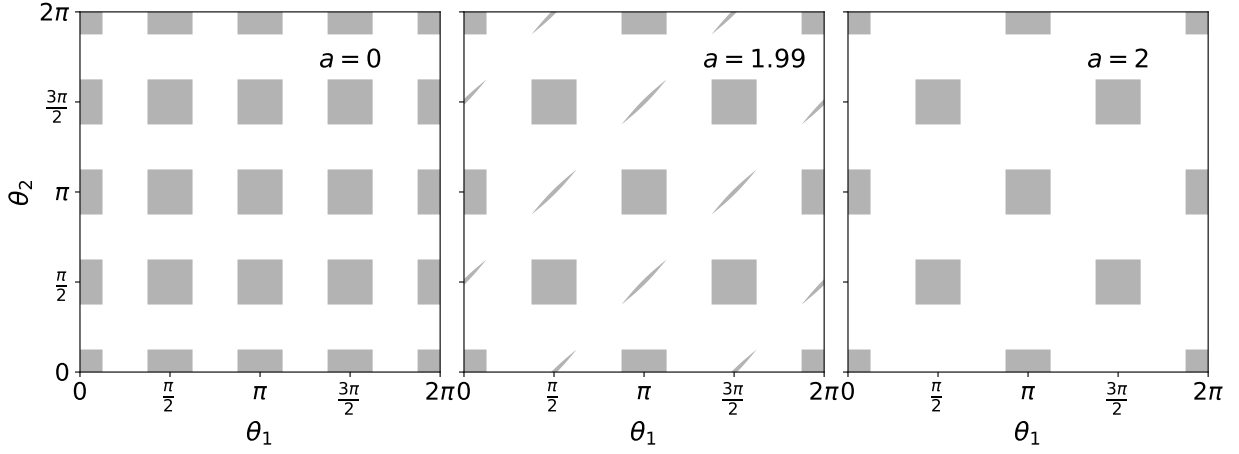


FIG. 16. ‘Sign’ of  $f_\phi(\theta_1, \theta_2)$  in the  $(\theta_1, \theta_2)$  plane for different  $a$  in (34). In the shaded regions,  $f_\phi(\theta_1, \theta_2) > 0$  for all  $\phi \in [0, \frac{\pi}{2}]$  such that  $e^{-S(z_1, z_2)} \rightarrow 0$  in the limit  $r \rightarrow \infty$ . For  $|a| > 2$ , analogous plots are identical to the right panel.

two diagonally opposite vertices of this cuboid. Thus, any other two points  $a'$  and  $b'$  whose arguments lie on diagonally opposite vertices of the same cuboid define an integration manifold within the same equivalence class of cycles. Moreover, the parallel shift of vertices within the  $G_i$  corresponds to a homotopy transformation and thus does not give rise to a different integration cycle. In other words, a single cuboid describes multiple (but equivalent) possible integration manifolds. Furthermore, if a cuboid is degenerate, i.e., if two or more of its vertices happen to lie within the same  $G_i$  (which is the case if one or more  $a_i = b_i$ ), the resulting integral is still well-defined but vanishes exactly and is thus not relevant for our purposes.

Let us demonstrate the idea, considering the class of two-dimensional theories defined in (34) with  $\lambda = 4$  as an example. After introducing polar coordinates and defining the angle  $\phi := \arctan\left(\frac{r_2}{r_1}\right) \in [0, \frac{\pi}{2}]$ , we can write the real part of  $S(z)$  as

$$\text{Re } S(z) = r^4 f_\phi(\theta_1, \theta_2), \quad (\text{A4})$$

with

$$f_\phi(\theta_1, \theta_2) = \cos^4(\phi) \left[ \cos(4\theta_1) + \tan^4(\phi) \cos(4\theta_2) + a \tan^2(\phi) \cos(2(\theta_1 + \theta_2)) \right]. \quad (\text{A5})$$

The problem of determining the regions  $G_i$  where  $e^{-S} \rightarrow 0$  (i.e.,  $\text{Re } S \rightarrow \infty$ ) as  $r \rightarrow \infty$  thus reduces to the problem of finding the regions in  $(\theta_1, \theta_2)$ -space in which  $f_\phi(\theta_1, \theta_2) > 0$  for all  $\phi \in [0, \frac{\pi}{2}]$ . We show these regions for three different values of the coupling parameter  $a$  in Fig. 16. As can be seen, the number  $N_G$  of regions  $G_i$  changes as  $a$  is varied. Indeed, we find  $N_G = 16$  if  $-2 < a < 2$  and  $N_G = 8$  otherwise, taking into account

the periodicity in both  $\theta_1$  and  $\theta_2$ . As is explained below, this fact results in a jump in the number of linearly independent integration cycles at  $a = \pm 2$ . The construction of the  $G_i$  in more general theories is analogous.

We remark at this point that the fact that  $f_\phi(\theta_1, \theta_2)$  must be positive for *all* values of  $\phi$  is important. Indeed, while one might naively expect to be able to consider the interval  $[0, \frac{\pi}{2}]$  only up to a set of measure zero, this is not true in general. In fact, without going into the details, we have found in the case  $a = 2$  that for  $\phi = \frac{\pi}{4}$ , corresponding to the line  $r_1 = r_2$ , a non-integrable singularity arises in the integral over certain cycles. Thus, simply omitting this point would lead to the wrong conclusion that there are 9 independent cycles for  $a = 2$ , when there are really only two, namely those unaffected by the aforementioned singularity. Following the above argument, the allowed integration cycles of (34) can now be represented as rectangles whose vertices all lie in different  $G_i$ . For  $a = 2$ , as seen in the right panel of Fig. 16, there are only two such rectangles, from which we conclude that the theory (37) has at most two independent integration cycles.

The final ingredient that we need in order to reduce the set of all possible integration cycles to a set of linearly independent ones is a generalization of the addition rule (13) for higher dimensions. With an arbitrary (possibly infinite) point  $c$ , such a generalization can be written as

$$\int_a^b d^d z = \sum_{x \in X} \text{sign}(x) \int_x^c d^d z, \quad (\text{A6})$$

where  $X$  is the set defined in (A3) and we have introduced the sign function on  $X$  as

$$\text{sign}(x) := \prod_{i=1}^d s_i, \quad s_i = \begin{cases} +1 & \text{if } x_i = a_i \\ -1 & \text{if } x_i = b_i \end{cases}. \quad (\text{A7})$$

With this, the increase in complexity when going beyond  $d = 1$  (where the number of independent integration cycles for an  $n$ -th-order-polynomial action is simply given

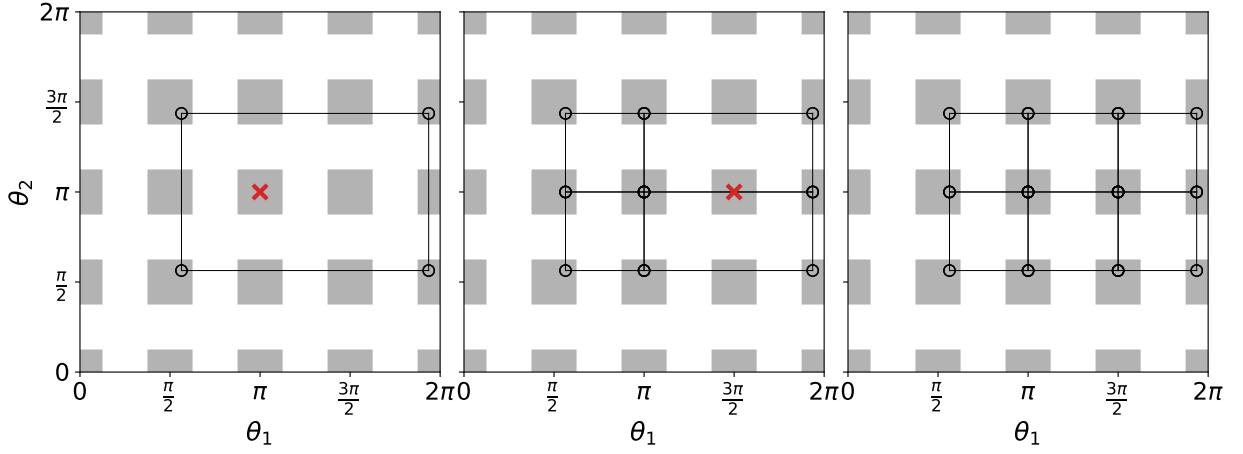


FIG. 17. As in the left panel of Fig. 16 but in addition we show how our algorithm can be used to decompose rectangles into smaller ones: Starting from the rectangle in the left panel, we choose a  $c$  in its interior (red cross) to obtain the four smaller rectangles shown in the center panel. The smaller two of these rectangles cannot be decomposed anymore, while for the other two we choose a  $c$  that lies on the side they share (red cross in the center panel). This gives rise to four additional rectangles, as seen in the right panel. The resulting six rectangles cannot be decomposed anymore, i.e., they are atomic, such that the algorithm has converged.

by  $n - 1$ ) can easily be appreciated. Indeed, while the right-hand side of (A6) consists of only two terms for  $d = 1$  (c.f. (13)), it involves  $2^d$  terms in general.

The graphical interpretation of (A6) is that one may decompose any integration cycle, i.e., any cuboid, into a sum (with appropriate signs) of all cuboids that share one vertex with the original cuboid and have the point  $c$  as its diagonally opposite vertex. This observation is at the heart of our counting algorithm.

Indeed, the underlying idea is to start with any cuboid that represents a valid integration cycle and use (A6) to decompose it into smaller and smaller cuboids. Here, by the ‘size’ of a cuboid we refer to its volume in  $\Theta_d$ . For instance, one could consider the smallest volume of all cuboids within the same equivalence class. Such a reduction can be accomplished by choosing the point  $c$  in (A6) to lie within (or on) the original cuboid, giving rise to  $2^d$  smaller cuboids, each of which one again tries to decompose further until convergence. Notice that this procedure might give rise to degenerate cuboids, which correspond to vanishing integrals and can thus simply be discarded. At the end of such an iterative procedure, one is left with a set of small cuboids that cannot be decomposed anymore and that we thus henceforth refer to as atomic. In other words, the original cuboid can be represented as a sum (with appropriate signs) of these atomic cuboids and such a decomposition in terms of atomics is possible for any given cuboid. Thus, the atomic cuboids constitute a basis for the cuboids, i.e., for integration cycles. Importantly, this algorithm is guaranteed to converge as the size of the involved cuboids decreases with every iteration step and there is a minimum size of cuboids for a given theory.

An example of how this algorithm works within the two-dimensional theory (34) with  $a = 0$  is shown in

Fig. 17, where the rectangle on the left plot is decomposed into atomic rectangles after two iteration steps. It is not hard to see that in total there are nine such atomic rectangles in this theory, from which we conclude that there are nine linearly independent integration cycles. The same is true for all  $|a| < 2$ , as can be seen, for instance, in the center plot of Fig. 16, where we consider  $a = 1.99$ . For  $a \geq 2$ , however, there are only two atomic rectangles. This is because eight of the regions  $G_i$  decrease in size as  $|a|$  increases from 0 to 2, causing them to disappear completely at  $a = 2$ , leaving only two independent cycles. Notice that this shrinking of the  $G_i$  also implies that not all possible integration manifolds that are valid cycles for  $a = 0$  are also valid for  $0 < a < 2$ . However, there is at least one representative out of each equivalence class that defines an allowed cycle for all  $|a| \leq 2$ . For instance, such a representative is given by the cuboid that connects the centers of four different  $G_i$ , see Fig. 16.

We note that this algorithm is capable of finding one particular set of linearly independent integration cycles. In practice, however, this basis is not always the most convenient to use, such that one may resort to using different sets instead, as is done, for instance, in Sec. VB. Nonetheless, it can be a helpful tool in determining the number of independent integration cycles to use, for instance, in a computer program and the generalization to higher dimensions  $d$  is straightforward. We also note that if one knows a set of possible integration cycles  $\gamma_j$  of a given theory and can furthermore compute expectation values of a sufficiently large set of observables  $\mathcal{O}_i$  along these cycles, then the rank of the matrix  $M$ , defined by  $M_{ij} := \langle \mathcal{O}_i \rangle_{\gamma_j}$ , also gives (a lower bound on) the number of independent integration cycles. For the cases studied in this work, we have verified that this method and the



above algorithm give consistent results.

### Appendix B: Testing the goodness of fits

In order to compute estimators for expectation values and uncertainties of the coefficients  $a_i$  in (10), we perform the least-squares fit analysis described in Sec. IV D 3. For the interpretation of results, however, assessing the goodness of such a fit is of fundamental importance. In this appendix, we shall be concerned with this question. In particular, our aim is to find a measure for the extent to which (10) is fulfilled. Thereby, we compare the observables  $\langle \mathcal{O} \rangle_{\text{CL}}$  measured in our complex Langevin simulations to the model predictions  $\sum_{i=1}^{N_\gamma} a_i \langle \mathcal{O} \rangle_{\gamma_i}$ , where the  $a_i$  are the coefficients resulting from the fit procedure and  $\langle \mathcal{O} \rangle_{\gamma_i}$  are the expectation values of observables  $\mathcal{O}$  along the integration cycles  $\gamma_i$ , which, in the models we investigate in this work, we can compute via numerical integration. As in Sec. IV D 3, however, we consider only real observables, such that what we are really concerned with is the deviation between the vectors  $\mathbf{y}$  and  $X\boldsymbol{\beta}$ , where  $\mathbf{y}$ ,  $X$  and  $\boldsymbol{\beta}$  are all defined in Sec. IV D 3.

To begin with, perhaps the most common goodness-of-fit test is the reduced  $\chi^2$  statistic. For this, one considers the vector of residuals, i.e.,  $\mathbf{y} - X\boldsymbol{\beta}$ , and computes the sum of their squares weighted by the (suitably normalized) covariance matrix of  $\mathbf{y}$ ,  $\Sigma$ , c.f., (24):

$$\chi^2 := (\mathbf{y} - X\boldsymbol{\beta})^T \Sigma^{-1} (\mathbf{y} - X\boldsymbol{\beta}). \quad (\text{B1})$$

The value of  $\chi^2$  is then compared to the effective number of (in this case: real) degrees of freedom,  $N_{\text{dof}} = 2N_{\mathcal{O}} - 2N_\gamma$ . In particular, one concludes that the fit is good (bad) if  $\chi^2 \approx N_{\text{dof}}$  ( $\chi^2 \gg N_{\text{dof}}$ ), while it is considered an overfit if  $\chi^2 < N_{\text{dof}}$ . The issue with this procedure, however, is that it relies on the residuals being Gaussian distributed. As we shall see below, this condition is not always met for our data, preventing us from using the standard reduced  $\chi^2$  statistic as a goodness-of-fit test in a straightforward way.

Instead, we follow [74] by studying the distribution of the weighted residuals directly. Under the assumption that the model is correct and the data are uncorrelated and follow a Gaussian distribution with known variances  $\sigma_i^2$ , then the residuals, weighted by  $1/\sigma_i$ , should follow a standard normal distribution. Since the data in our simulations are not uncorrelated, however, we first decorrelate the measurements by performing a so-called whitening transformation. There are infinitely many ways to do this in general [75]. Here, we consider one particular method, namely the *ZCA-cor* whitening transformation, retaining the maximal amount of component-wise correlation between the original and the whitened data [75]. In this approach, the whitened residuals are defined as

$$\mathbf{x} = W^{\text{ZCA-cor}} (\mathbf{y} - X\boldsymbol{\beta}), \quad (\text{B2})$$

with the whitening matrix

$$W^{\text{ZCA-cor}} = P^{-1/2} V^{-1/2}. \quad (\text{B3})$$

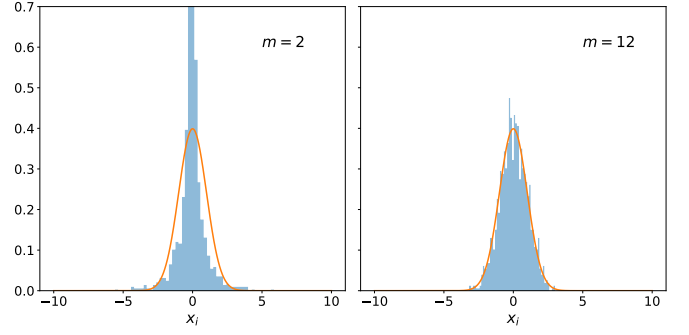


FIG. 18. Distribution of the whitened residuals  $x_i$  in (B2) obtained from complex Langevin simulations of the model (26) with  $\lambda = e^{5i\pi/6}$  and a kernel of the form (28) for two different values of the integer  $m$ . The histograms have been normalized such that they sum to 1 and a normal distribution with zero mean and unit variance is shown for comparison.

Here, the matrices  $P$  and  $V$  are defined such that  $\Sigma = V^{1/2} P V^{1/2}$ , where  $\Sigma$  again denotes the covariance matrix of the measurements  $\mathbf{y}$ , but now it is computed as an average over simulation runs and not additionally normalized. In other words,  $P$  corresponds to the correlation matrix, while  $V$  is the diagonal variance matrix. Similarly,  $\boldsymbol{\beta}$  in (B2) denotes the average over runs as well. Note that the whitening matrix is computed from the full data set once, while we compute one vector  $\mathbf{x}$  from  $\mathbf{y}$  for every simulation run, leaving us with a total  $2N_{\mathcal{O}}N_{\text{runs}}$  data points  $x_i$ . Indeed, we find each  $\mathbf{x}$  to be perfectly uncorrelated, such that we may study the distribution of the  $x_i$  as a test for the goodness of our fitting procedure.

Two exemplary such distributions that we obtain in the theory (26) with  $\lambda = e^{5i\pi/6}$  for a kernel of the form (28) with  $m = 2$  and  $m = 12$ , respectively, are shown in Fig. 18. Indeed, we see that the distribution closely resembles a Gaussian with zero mean and unit variance for  $m = 12$ , where we know boundary terms to be consistent with zero (c.f. Fig. 5), whereas there is a substantial deviation for  $m = 2$ , where boundary terms are nonzero.

Lastly, in order to quantify the deviation of the produced distribution from a standard normal distribution, we employ the Shapiro–Wilk test [76], from which we may compute the associated  $p$ -value. This quantity is the probability of measuring the observed distribution under the assumption that the null hypothesis, i.e., that the whitened residuals are drawn from a standard Gaussian distribution, is correct. A small  $p$ -value thus indicates that the observed outcome is likely incompatible with the residuals being Gaussian distributed. In turn, this means from that large (small)  $p$ -values within the Shapiro–Wilk test, we may conclude that the fit for the coefficients  $a_i$  is good (bad). As a threshold, we use the commonly employed value  $p = 0.05$ .

For the model (26) with  $\lambda = e^{5i\pi/6}$ , we show the  $p$ -value as a function of the kernel parameter  $m$  in Fig. 19. Comparing this result to Fig. 5, we observe a clear correlation between the presence of boundary terms and  $p$ -



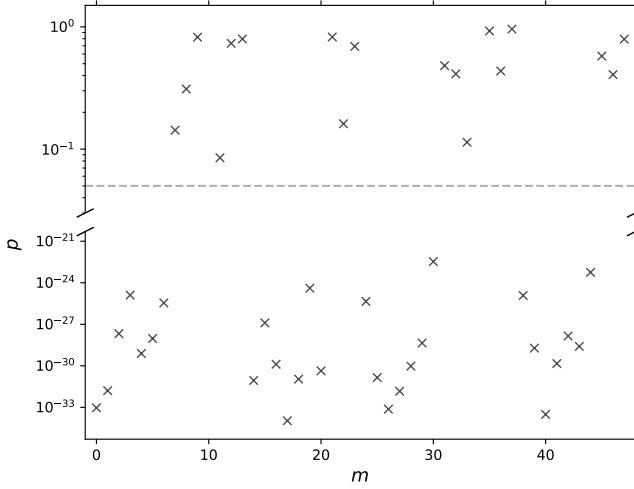


FIG. 19.  $p$ -value of a Shapiro–Wilk normality test applied to the whitened residuals obtained from complex Langevin simulations of the model (26) with  $\lambda = e^{5i\pi/6}$ . The horizontal axis is the kernel parameter  $m$  in (28) and the threshold value 0.05 is shown as the horizontal dashed line. Notice the interrupted vertical axis and the logarithmic scale.

values (many orders of magnitude) below 0.05. This is, in fact, true in all of our simulations, both in one and two dimensions. We have also experimented with different whitening transformations in (B2) and obtained consistent results. In conclusion, we find the approach presented here to provide a viable criterion for assessing the goodness of our least-squares fits in contrast to the reduced  $\chi^2$  statistic.

- 
- [1] L. L. Salcedo and E. Seiler, *J. Phys. A* **52**, 035201 (2019), [arXiv:1809.06888 \[math-ph\]](#).
  - [2] Y. Aoki, G. Endrődi, Z. Fodor, S. D. Katz, and K. K. Szabó, *Nature* **443**, 675 (2006), [arXiv:hep-lat/0611014](#).
  - [3] M. Troyer and U.-J. Wiese, *Phys. Rev. Lett.* **94**, 170201 (2005), [arXiv:cond-mat/0408370](#).
  - [4] P. de Forcrand, S. Kim, and T. Takaishi, *Nucl. Phys. B – Proc. Suppl.* **119**, 541 (2003), [arXiv:hep-lat/0209126](#).
  - [5] A. Goksch, *Phys. Rev. Lett.* **61**, 2054 (1988).
  - [6] S. Chandrasekharan, *PoS (LATTICE 2008)*, 003 (2009), [arXiv:0810.2419 \[hep-lat\]](#).
  - [7] G. Parisi, *Phys. Lett. B* **131**, 393 (1983).
  - [8] J. R. Klauder, *J. Phys. A* **16**, L317 (1983).
  - [9] M. Cristoforetti, F. Di Renzo, and L. Scorzato (Aurora-Science Collaboration), *Phys. Rev. D* **86**, 074506 (2012), [arXiv:1205.3996 \[hep-lat\]](#).
  - [10] M. C. Bañuls, K. Cichy, J. I. Cirac, K. Jansen, and S. Kühn, *PoS (LATTICE2018)*, 022 (2019), [arXiv:1810.12838 \[hep-lat\]](#).
  - [11] M. Alford, A. Kapustin, and F. Wilczek, *Phys. Rev. D* **59**, 054502 (1999), [arXiv:hep-lat/9807039v1](#).
  - [12] C. Allton, S. Ejiri, S. J. Hands, O. Kaczmarek, F. Karsch, E. Laermann, C. Schmidt, and L. Scorzato, *Phys. Rev. D* **66**, 074507 (2002), [arXiv:hep-lat/0204010](#).
  - [13] G. Parisi and Y.-S. Wu, *Sci. Sin.* **24**, 483 (1981).
  - [14] P. Damgaard and H. Hüffel, *Phys. Rep.* **152**, 227 (1987).
  - [15] M. Namiki, *Prog. Theor. Phys. Suppl.* **111**, 1 (1993).
  - [16] F. Karsch and H. W. Wyld, *Phys. Rev. Lett.* **55**, 2242 (1985).
  - [17] B. Söderberg, *Nucl. Phys. B* **295**, 396 (1988).
  - [18] H. Gausterer and S. Lee, *J. Stat. Phys.* **73**, 147 (1992), [arXiv:hep-lat/9211050](#).
  - [19] K. Okano, L. Schülke, and B. Zheng, *Prog. Theor. Phys. Suppl.* **111**, 313 (1993).
  - [20] J. Ambjørn and S. K. Yang, *Phys. Lett. B* **165**, 140 (1985).
  - [21] J. Ambjørn, M. Flensburg, and C. Peterson, *Nucl. Phys. B* **275**, 375 (1986).
  - [22] L. L. Salcedo, *Phys. Lett. B* **304**, 125 (1993).
  - [23] K. Fujimura, K. Okano, L. Schülke, K. Yamagishi, and B. Zheng, *Nucl. Phys. B* **424**, 675 (1994), [arXiv:hep-th/9311174](#).
  - [24] J. Berges and I.-O. Stamatescu, *Phys. Rev. Lett.* **95**, 202003 (2005), [arXiv:hep-lat/0508030](#).
  - [25] J. Berges, S. Borsányi, D. Sexty, and I.-O. Stamatescu, *Phys. Rev. D* **75**, 045007 (2007), [arXiv:hep-lat/0609058](#).
  - [26] G. Aarts, F. A. James, E. Seiler, and I.-O. Stamatescu, *Phys. Lett. B* **687**, 154 (2010), [arXiv:0912.0617 \[hep-lat\]](#).
  - [27] E. Seiler, D. Sexty, and I.-O. Stamatescu, *Phys. Lett. B* **723**, 213 (2013), [arXiv:1211.3709 \[hep-lat\]](#).
  - [28] D. Sexty, *Phys. Lett. B* **729**, 108 (2014), [arXiv:1307.7748 \[hep-lat\]](#).
  - [29] D. Sexty, *Nucl. Phys. A* **931**, 856 (2014), [arXiv:1408.6767 \[hep-lat\]](#).
  - [30] G. Aarts, E. Seiler, D. Sexty, and I.-O. Stamatescu, *Phys. Rev. D* **90**, 114505 (2014), [arXiv:1408.3770 \[hep-lat\]](#).
  - [31] Z. Fodor, S. D. Katz, D. Sexty, and Török, *Phys. Rev. D* **92**, 094516 (2015), [arXiv:1508.05260 \[hep-lat\]](#).
  - [32] F. Attanasio, B. Jäger, and F. P. G. Ziegler, [arXiv:2203.13144 \[hep-lat\]](#).
  - [33] G. Aarts, F. Attanasio, B. Jäger, and D. Sexty, *JHEP* **2016**, 087, [arXiv:1606.05561 \[hep-lat\]](#).
  - [34] C. E. Berger, L. Rammelmüller, A. C. Loheac, F. Ehmann, J. Braun, and J. E. Drut, *Phys. Rep.* **892**, 1 (2021), [arXiv:1907.10183 \[cond-mat\]](#).
  - [35] G. Aarts, E. Seiler, and I.-O. Stamatescu, *Phys. Rev. D* **81**, 054508 (2010), [arXiv:0912.3360 \[hep-lat\]](#).
  - [36] G. Aarts, F. A. James, E. Seiler, and I.-O. Stamatescu, *Eur. Phys. J. C* **71**, 1756 (2011), [arXiv:1101.3270 \[hep-lat\]](#).

- [37] L. L. Salcedo, *Phys. Rev. D* **94**, 114505 (2016), [arXiv:1611.06390 \[hep-lat\]](#).
- [38] K. Nagata, J. Nishimura, and S. Shimasaki, *Phys. Rev. D* **94**, 114515 (2016), [arXiv:1606.07627 \[hep-lat\]](#).
- [39] M. Scherzer, E. Seiler, D. Sexty, and I.-O. Stamatescu, *Phys. Rev. D* **99**, 014512 (2019), [arXiv:1808.05187 \[hep-lat\]](#).
- [40] M. Scherzer, E. Seiler, D. Sexty, and I.-O. Stamatescu, *Phys. Rev. D* **101**, 014501 (2020), [arXiv:1910.09427 \[hep-lat\]](#).
- [41] E. Seiler, D. Sexty, and I.-O. Stamatescu, *Phys. Rev. D* **109**, 014509 (2024), [arXiv:2304.00563 \[hep-lat\]](#).
- [42] E. Witten, *AMS/IP Stud. Adv. Math.* **50**, 347 (2011), [arXiv:1001.2933 \[hep-th\]](#).
- [43] E. Witten, [arXiv:1009.6032 \[hep-th\]](#).
- [44] M. D. Wilkinson et al., *Sci. Data* **3**, 160018 (2016).
- [45] L. L. Salcedo, *J. Math. Phys.* **38**, 1170 (1997), [arXiv:hep-lat/9607044](#).
- [46] D. Weingarten, *Phys. Rev. Lett.* **89**, 240201 (2002), [arXiv:quant-ph/0210195](#).
- [47] L. L. Salcedo, *J. Phys. A* **40**, 9399 (2007), [arXiv:0706.4359 \[hep-lat\]](#).
- [48] N. M. Lampl and D. Sexty, [arXiv:2309.06103 \[hep-lat\]](#).
- [49] D. Alvestad, R. Larsen, and A. Rothkopf, *JHEP* **2023**, 057, [arXiv:2211.15625 \[hep-lat\]](#).
- [50] D. Alvestad, A. Rothkopf, and D. Sexty, *Phys. Rev. D* **109**, L031502 (2024), [arXiv:2310.08053 \[hep-lat\]](#).
- [51] M. W. Hansen and D. Sexty, *Phys. Rev. D* **111**, 054508 (2025), [arXiv:2405.20709 \[hep-lat\]](#).
- [52] M. Mandl, M. W. Hansen, E. Seiler, and D. Sexty, *PoS (LATTICE2024)*, 059 (2025), [arXiv:2410.13423 \[hep-lat\]](#).
- [53] S. García, Z. Guralnik, and G. S. Guralnik, [arXiv:hep-th/9612079](#).
- [54] G. Guralnik and C. Pehlevan, *Nucl. Phys. B* **811**, 519 (2009), [arXiv:0710.3756 \[hep-th\]](#).
- [55] G. Guralnik and Z. Guralnik, *Ann. Phys.* **325**, 2486 (2010), [arXiv:0710.1256 \[hep-th\]](#).
- [56] M. W. Hansen, M. Mandl, E. Seiler, and D. Sexty, *Zenodo* [10.5281/zenodo.14517088](#) (2024).
- [57] M. W. Hansen, M. Mandl, E. Seiler, and D. Sexty, *Zenodo* [10.5281/zenodo.14517265](#) (2024).
- [58] A. Ukawa and M. Fukugita, *Phys. Rev. Lett.* **55**, 1854 (1985).
- [59] P. L'Ecuyer, R. Simard, E. J. Chen, and W. D. Kelton, *Oper. Res.* **50**, 1073 (2002).
- [60] G. E. P. Box and M. E. Muller, *Ann. Math. Statist.* **29**, 610 (1958).
- [61] NVIDIA, P. Vingelmann, and F. H. Fitzek, *CUDA, release: 10.2.89* (2020).
- [62] H. Okamoto, K. Okano, L. Schülke, and S. Tanaka, *Nucl. Phys. B* **324**, 684 (1989).
- [63] G. Aarts, *Phys. Rev. D* **88**, 094501 (2013), [arXiv:1308.4811 \[hep-lat\]](#).
- [64] G. Aarts, L. Bongiovanni, E. Seiler, and D. Sexty, *JHEP* **2014**, 159, [arXiv:1407.2090 \[hep-lat\]](#).
- [65] K. Boguslavski, P. Hotzy, and D. I. Müller, *SciPost Phys.* **18**, 092 (2025), [arXiv:2412.02396 \[hep-lat\]](#).
- [66] K. Okano, L. Schülke, and B. Zheng, *Phys. Lett. B* **258**, 421 (1991).
- [67] G. van Rossum and J. de Boer, *CWI Quarterly* **4**, 283 (1991).
- [68] S. van der Walt, S. C. Colbert, and G. Varoquaux, *Comput. Sci. Eng.* **13**, 22 (2011).
- [69] SciPy 1.0 Contributors: P. Virtanen, R. Gommers et al., *Nature Methods* **17**, 261 (2020).
- [70] W. McKinney, *Proceedings of the 9th Python in Science Conference (Scipy 2010)*, 51 (2010).
- [71] J. D. Hunter, *Comput. Sci. Eng.* **9**, 90 (2007).
- [72] F. Cramer, *Zenodo* [10.5281/zenodo.8409685](#) (2023).
- [73] Wolfram Research, Inc., *Mathematica, Version 13.3*.
- [74] R. Andrae, T. Schulze-Hartung, and P. Melchior, [arXiv:1012.3754 \[astro-ph\]](#).
- [75] A. Kessy, A. Lewin, and K. Strimmer, *Am. Stat.* **72**, 309 (2018), [arXiv:1512.00809 \[stat\]](#).
- [76] S. S. Shapiro and M. B. Wilk, *Biometrika* **52**, 591 (1965).